Erik Løvdahl

A Discrete Element Method Study of Shear Localisation in Granular Material

July 2020

NTNU
Norwegian University of
Science and Technology

Master's thesis

2020

Erik Løvdahl

Master's thesis

NTNU
Norwegian University of
Science and Technology
Faculty of Engineering
Department of Civil and Environmental Engineering

NTNU
Norwegian University of
Science and Technology

NTNU
Norwegian University of
Science and Technology

A Discrete Element Method Study of Shear Localisation in Granular Material

Erik Løvdahl

Civil and Environmental Engineering
Submission date: July 2020
Supervisor: Gudmund Reidar Eiksund
Co-supervisor: Steinar Nordal

Norwegian University of Science and Technology
Department of Civil and Environmental Engineering

Preface

This master thesis was written as the concluding work of an integrated five year master's degree in civil and environmental engineering at NTNU in Trondheim. It was written during the spring semester of 2020.

Investigation into subjects regarding the use of the Discrete Element Method in geotechnics was proposed by my co-supervisor Steinar Nordal. The subject was determined as the consequence of an initial study conducted into the capabilities of DEM-software Yade. Part of the resulting report of this work is included in chapter 2.

I would like to thank professors Gudmund Eiksund and Steinar Nordal for their guidance during this thesis work. I would also like to thank NTNU, and more specifically Kenneth Sundli for providing me with server capacity needed for running the simulations.

Oslo, 15.07.2020

Erik Løvdahl

Abstract

A flexible boundary condition is developed for simulated triaxial and biaxial compression tests using the Discrete Element Method (DEM) software Yade. The method performs simulations of individual particles in granular material. With simple contact laws and physics at the particle scale, DEM is capable of producing complex behavior at the macroscopic scale.

The triaxial test is the industry standard in determining soil behaviour, and is utilised in calibration of material behaviour in DEM. Differences in sample response for rigid and flexible boundaries are assessed, and properties of shear localisation in plane strain tests are examined. Sample behaviour with rigid and flexible boundaries is largely consistent for the triaxial tests. The calibration results imply that the addition of flexible borders have limited effect on peak friction angle. The stiffness is however impacted significantly.

The shear localisation results are congruent with the descriptions of shear band behaviour found in the literature, showing force chain buckling in connection with localised dilatancy and rotation in the bands. Shear band orientations closely match the theoretically expected orientation with frictionless platens, but differ with the rough condition.

The effects of end conditions on shear banding in the simulated plane strain tests are examined. Rough and frictionless end conditions lead to almost identical peak stress, but different mechanisms of failure. Frictionless end conditions suggest a more brittle failure and a tendency of developing a clearly defined, singular shear band. Rough end conditions lead to development of two diagonally crossing bands. With rigid boundaries these mechanisms develop simultaneously, with no clear primary and secondary band. The flexible boundaries show development of one highly developed primary band and a secondary band. The tests show a less abrupt reduction of stress in the post-peak region suspected to be because of a somewhat higher stability in the failure mechanism of double bands. These show different orientations with the principal stress directions, with the primary band at a steeper angle.

Sammendrag

En fleksibel grensebetingelse er implementert for simulerte trykktester i diskret elementmetode (DEM) programmet Yade. DEM simulerer individuelle partikler i et granulært materiale. Med enkle kontaktlover og fysikk på partikkelnivå, fremkommer kompleks materialoppførsel på makronivå.

Treaksialtest er en av de mest anerkjente og pålitelige laboratorietestene som brukes for å bestemme jordoppførsel, og brukes også i kalibrering av DEM. Forskjeller i materialoppførsel ved bruk av stive og fleksible grensebetingelser er undersøkt. Egenskaper ved utvikling av skjærbånd er også studert. Maksimal mobilisert friksjonsvinkel viser liten forskjell mellom plan tøynings- og treaksialtest kjørt med fleksible og stive grensebetingelser. Målt materialstivhet viser derimot signifikant påvirkning.

Egenskapene vist ved skjærbåndutvikling følger i stor grad oppførsel beskrevet i litteraturen, med eksempler på utknekking av kraftsøyler og påfølgende dilatans og partikkelrotasjon i skjærbånd. Helningsvinklene på skjærbåndene følger teorien godt ved bruk av glatte lastplater, men ikke ved friksjon langs platene. Det blir utført tester for å bestemme effekten av helt ru og helt friksjonsløse endeplater. Testene viser nesten identisk maksimal friksjonsvinkel for begge endebetingelsene, men ulike bruddmekanismer. Glatte endeplater viser tendenser til sprøbruddsoppførsel, og utvikler et enkelt, klart definert skjærbånd i materialet. Ru endeplater forhindrer utglidning av endene av prøven og fører til utvikling av to kryssende skjærbånd. Med stive grenser utvikles disse båndene parallelt, mens de fleksible grensene fører til økt lokalisering i et bestemt primærbånd. Disse testene viser også en mindre tendens til sprøbruddsoppførsel trolig på grunn av høyere stabilitet med to skjærbånd. Primærbåndet har brattere helning enn det sekundære.

Contents

List of Figures

List of Tables

List of Symbols

μ - interparticle friction angle
φ_p - peak mobilized friction angle
φ_{cv} - critical state friction angle
ψ - dilatancy angle
ν - poisson ratio
θ - measured shear band orientation angle
θ_C - Mohr Coulomb orientation angle
θ_R - Roscoe orientation angle
σ_1 - major principal normal stress
σ_2 - intermediate principal normal stress
σ_3 - minor principal normal stress
ε_1 - major principal normal strain
ε_2 - intermediate principal strain
ε_3 - minor principal strain
ρ - solid density
ε_V - volumetric strain
e - void ratio
n - porosity
λ - damping ratio

Chapter 1

Introduction

1.1 Motivation

Shear localisation or shear banding is a commonplace phenomena in material sciences. It manifests itself at different scales and in many different materials. In soil mechanics, rupture surfaces as failure mechanisms are well known as the consequence of this localisation.

While the macroscopic consequence of shear localisation is visible with the naked eye, the mechanisms acting on the particle scale remained a subject of speculation for decades. Through the implementation of techniques of particle observation such as x-ray computed tomography and numerical methods, the particle effects are being revealed (Kawamoto et al., 2017), (Oda & Kazama, 1998).

The research community has been searching for a continuum mechanical approach for describing shear banding since the seventies (Desrues & Andò, 2015). The phenomenon does however not lend itself well to a continuum mechanical approach in soils due to the inherent discontinuity of granular matter. For this, the Discrete Element Method is much more suitable.

The Discrete Element Method (DEM) was proposed by Cundall and Strack (1979) as a tool to simulate granular material modelled as assemblies of disks in two dimensions. Since then, DEM-software has come a long way with capabilities such as three dimensional simulations of crushable polyhedral particles and pore-scale fluid flow (Eliáš, 2014), (Chareyre et al., 2011).

DEM differs from other numerical methods like the Finite Element Method, in that it simulates the individual particles of a material. Each particle has a position and orientation and interacts with other bodies. Cundall argues that through the use of simple contact laws and physics at the particle scale, all manner of complex behaviour arise at the macro scale without the need of extensive constitutive modeling.

In recent years DEM has gained increased popularity and functionality, and many programs offer coupling with Computational Fluid Dynamics (CFD) and the Finite Element Method (FEM). DEM is today considered a valuable tool for simulation of particle behaviour in material sciences.

Before use, DEM programs need to perform calibration tests to confirm material behaviour in line with physical material behaviour. This can normally be done by calibration with the gold standard in laboratory investigation of geomaterials for engineering - the triaxial test. However, in the conventional triaxial test, lateral stress is controlled through water pressure acting on the membrane clad surface of the sample. This allows variable lateral deformation over the height of the sample. The convention in DEM studies is the use of triaxial tests performed with rigid boundaries (Kozicki et al., 2012). The boundaries are stress controlled but inhibit said variable lateral deformation, restricting shear banding.

1.2 Scope and objectives

This thesis will study the effects of boundary conditions on traxial and biaxial compressions tests with DEM simulations. The open-source DEM software Yade will be used for this purpose. The focus of this thesis will therefore be to create a flexible boundary condition in order to study the properties of shear bands and the impact of flexible boundaries on simulated compression tests.

The objectives are the following:

- Develop a flexible boundary condition for a cubic sample.
- Determine the differences in rigid and flexible boundary conditions for compression tests.
- Examine particle behaviour inside shear bands.
- Determine how load platen roughness influence the shear localisation development.

1.3 Structure

The thesis is structured as follows:

Chapter 2 includes an overview of the DEM formulation in Yade, followed by a literature review describing general theory relevant for the objectives in this thesis. Shear banding is given particular attention.

Chapter 3 includes all details related to the development of the membrane, sample and the data evaluation features. It also includes descriptions of the given input parameters for the simulations.

Chapter 4 documents the calibration of input parameters of the compression tests. It includes comparisons of triaxial tests using both flexible and rigid boundaries. The results are discussed as they are presented.

Chapter 5 describes the shear localisation tests. The results from plane strain shear localisation tests will be presented and discussed, evaluating the shear banding behaviour with different boundary conditions.

Chapter 6 involves a general discussion of the results and limitations of the testing procedures.

The Yade scripts developed for this thesis are included in the separate appendix file.

Chapter 2

Theory

Chapter 2.1 is based on descriptions found in the Yade documentation (Šmilauer & Chareyre, 2015) where not explicitly stated otherwise. Moreover, the formulations of section 2.1 and parts of section 2.2 are included from the previous work of the author (Løvdahl, 2020).

2.1 DEM implementation in Yade

User input in Yade is given in the Python programming language, while the engine is programmed in C++ using a modular design. Many different contact laws, material models and particle types are available, targeting different applications. The following section offers brief descriptions of the use of the most basic modules in Yade.

The Discrete Element Method is based on an iterative loop between Newton's second law of motion and a force-displacement relation for the given particle types. The DEM implementation in Yade can roughly be described as a cycle with the following steps:

- Course collision detection of simulation elements
- Precise contact detection
- Force calculations from overlaps and stiffness formulations
- Application of Newton's second law of motion to particles with explicit time integration

Each sphere is modeled with six degrees of freedom - translation and rotation in the three dimensions. Each contact between a pair of particles also reduce down to six degrees of freedom to describe all modes of strain while in contact.

Collision and contact detection

To reduce computation time, Yade uses at first a courser method of determining potential collisions and subsequently refines the accuracy down to identify contacts precisely. The interactions may be between spheres, walls, facets, clumps or any other bodies interacting in the simulation.

Force calculation

Inter-particle forces are determined as the result of the overlap between particles corresponding to the deformations of the particles. This is termed "the soft particle" approach where the particle geometry remain unchanged and strains and forces are quantified by the overlaps. Precise modelling of particle deformation is very computationally expensive and is deemed unnecessary at sufficiently high stiffness levels.

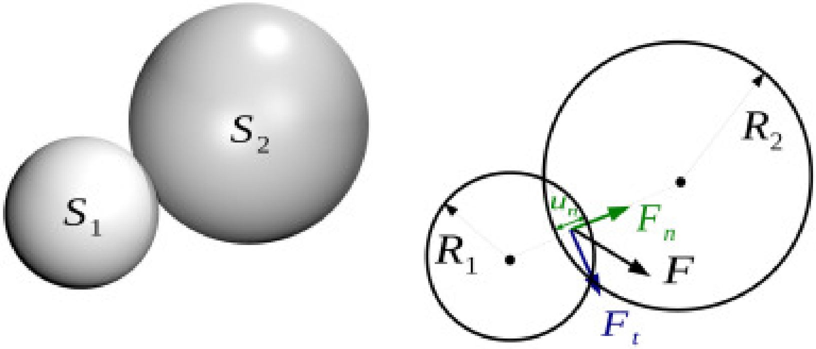

(a) (b)

Figure 2.1: Sphere-sphere interaction through overlaps (Effeindzourou et al., 2016).

The normal and tangential stiffness parameters K_N and K_S are calculated as functions of input stiffness E and radius of particles in a given interaction:

$$K_N = 2\frac{E_1 r_1 E_2 r_2}{E_1 r_1 + E_2 r_2} \tag{2.1}$$

The tangential or shear stiffness is given as a fraction of the normal stiffness K_N with the parameter ν:

$$\nu = \frac{K_T}{K_N} \tag{2.2}$$

The input parameter ν is shown to be proportional to the macroscopic poisson ratio and E is proportional to macroscopic youngs modulus(Kozicki et al., 2012).

By evaluating the strains and stiffness in each interaction the normal and tangential forces can respectively be calculated each cycle. Force from the particle strain is calculated as:

$$\vec{F_N} = K_N \cdot u_N \cdot \vec{n} \tag{2.3}$$

$$\vec{F_T} = K_T \cdot \vec{u_T} \tag{2.4}$$

F_N is the normal force, F_S the tangential force between particles and $\vec{n}$ is the normal vector of the particle contact. The force is then decomposed into reference directions and added up for all contacts for each object. The shear forces lead to a torsional force that is evaluated for angular motion of the particles.

The critical limit for the shear force is formulated after the classical Mohr-Coulomb relation:

$$F_S - F_N \cdot tan(\mu) \leq 0 \tag{2.5}$$

Where μ is the inter-particle friction angle. Frictional sliding in grain interaction occurs as implied when F_T surpasses the given criteria. During sliding the friction coefficient is kept equal to the maximum static friction.

For clumps composed of multiple spheres, collision detection is run for each of the individual clump members. The strain and forces are also calculated individually, but in the motion integration phase the forces and torques are converted to be applied to the clump acting as one. No relative displacement is allowed between the particles in a clump, making it behave as a rigid body.

Material models

Material models are used to determine particle behaviour. Each material class contain the necessary parameters for calculating material behaviour. Each particle has therefore a specified general material connected to it for use in the calculations.
As Yade is an open-source, highly modular software, there exists a multitude of different material models for simulating different behaviour.

The simplest model is the "FrictMat" model for cohesionless soils, which includes the minimum of parameters required in the calculation loop presented above. The material input parameters are particle stiffness and friction, solid density and the normal to shear stiffness ratio, labeled "poisson". It can simulate dry, granular material through the procedure described above.

A simple model for cohesive soils is the "CohFrictMat" model, extending the capabilities of FrictMat. It includes all the given input parameters from FrictMat and includes multiple new associated with cohesive soils and rolling resistant particles. Some of the additional parameters are normal and shear cohesion as values of minimum tensile and shear capacities at zero normal compressive stress. It also includes the option of applying rotational resistance for rolling (bending) and twisting (torsion) as well a plastic limit for the corresponding rotational strengths. It also includes capabilities of simulating brittle material failure with an option of disabling cohesion for all new contacts if cohesive capacity is exceeded.

Motion integration, timestep, stability

Each particle position, orientation and the corresponding velocities are tracked continuously. The particle motions are then updated at every iteration cycle through the use of explicit integration.

The time steps have to be small enough to warrant the assumption of constant accelerations and velocities at each step to ensure meaningful results. The critical timestep is calculated on the basis of the wave propagation speed in the defined material to ensure that the explicit integration scheme captures all particle accelerations and movements with adequate precision.

$$\Delta t_{cr} = min(R_i)\sqrt{\frac{\rho_i}{E_i}} \tag{2.6}$$

Damping

The numerical damping is a non-viscous damping as suggested by Cundall (1987). It increases energy dissipation by frictional damping in the model. It works by amplifying forces that work in the opposite direction of particle motion and decrease the forces that accelerate the particles in the direction of motion. This is entirely non-physical and unsuitable for dynamic problems, but increases the stability and performance of quasi-static simulations with low impact on the validity of the generated results.
The damping amplifies or decreases forces according to:

$$\frac{(\Delta F)_{d_w}}{F_w} = -\lambda \cdot sgn(F_w \dot{u}_w)\,, \quad w \in \{x, y, z\} \tag{2.7}$$

Where λ is the damping ratio, F_w the force and $\dot{u}_w$ the velocity in direction w.

2.2 Literature review

The following sections will include general DEM theory applicable to the topics discussed in this master thesis. Of special note being shear band characteristics and simulation boundary conditions.

2.2.1 Standard boundary conditions

There are mainly two types of boundaries introduced in Yade: Boundaries consisting of wall elements and periodic boundaries.

Periodic boundaries can efficiently model large soil volumes by repeating the space through the defined boundary such that a particle moving out through the boundary of the soil box is inserted on the opposite side. This is utilising a small representative volume element (RVE) to represent the aggregate material behaviour for homogeneous stress conditions. The sample is strained through decreasing the dimensions of the periodic cell, thus decreasing the available space between the grains and effectively increasing the inter-particle stresses.

Periodic boundaries are however limited to large homogeneous geometry and periodically repeating phenomena as it cannot represent localized effects correctly. This makes it unsuitable for simulating shear banding effects likely to occur as failure mechanisms in real triaxial testing(Kruyt & Rothenburg, 2006).

The other common set of boundaries implemented in Yade are the use of wall elements. These elements are assigned material properties in the same way as particles to allow sphere-wall interactions. The stiffnesses given as input in this case also give tangential and normal stiffness.

2.2.2 Flexible boundaries

Neither the periodic boundaries nor the wall boundaries can effectively present shear localization in the triaxial simulations due to the restrictive kinematics. For this, a flexible condition is required.

Three categories of membrane modelling methods discussed in (Qu et al., 2019) are presented. They are labeled:

- Stacked wall elements
- Equivalent force algorithms
- Particle membrane methods

Stacked walls construct membranes consisting of rigid planar surfaces stacked vertically to allow for lateral deformation over the height. These surfaces are stress controlled to keep the stress constant by allowing lateral deformation. They do not however, allow variable deformation of the width. They also require precise control of the deformation characteristics in order to simulate a membrane.

Equivalent force algorithms replace the membrane by applying force on the outmost particles in the sample. Introduced by Bardet and Proubet (1991). This method requires precise detection of boundary particles and determination of the equivalent boundary forces.

Particle membrane methods model the membrane as connected spherical particles and apply the lumped confining stress as forces on these known particles. One solution to this is presented in a paper by Kozicki et al. (2014). The spheres that make up the mesh are free to move relative to the other spheres in the structure, and can thus follow the deformation of the sample even for localised effects. As all defined outer particles are known, there is no need to develop algorithms to determine the outermost particles. Differs from real membrane in the sense that it is discontinuous, however this is of less impact with sufficiently small particles used in the membrane compared to sample particles. This entails of course greater computational cost with a large particle count in the membrane.

Another method can be added to this list, namely the use of flexible elements discussed below.

Flexible elements
Flexible elements in Yade were implemented by Effeindzourou et al. (2016) and the following section is based on this paper where not specified otherwise. The flexible elements consist of spheres called grid nodes, cylindrical elements called grid connections and area elements called P-facets.

The flexible elements utilise a Minkowsky sum of geometries to represent the different shapes. In order to generate a complete P-facet, the structure is set by generating grid nodes and then designating connections between them in a grid. The area elements can then be added to connected triangular grid elements to complete the structure. By using only grid connections and grid nodes, one can represent meshes like flexible nets and wire mesh materials. The cylinder elements were also successfully used in simulating plant root reinforcement of soil in direct shear tests (Bourrier et al., 2013).

These smooth elements offer better control over the interaction with soil particles as opposed to the common method of linking adhesive spheres together to form flexible elements. The linked spheres exhibit higher friction with the surrounding soil naturally due to the large roughness of the chains and the calculation of interactions in DEM (Bourrier et al., 2013).

Each individual cylinder element is kept geometrically rigid, thus cannot represent bending alone, but are able to rotate relative to adjoining elements. The connection can deform only in the longitudinal direction. Each individual P-facet element is also as a consequence kept planar. Through the use of multiple elements and applied moment resistance in the element nodes one can simulate beam elements. The deformations of the elements are depending on the translation and rotation of the two nodes of each given cylinder. Mass and force from the cylinder is lumped into the two spherical nodes. These beam elements can represent tension and shear forces as well as bending and twisting moments.

Contact detection is solved through the use of the existing sphere-sphere contact detection in Yade. For any potential interaction along the P-facet bodies, a virtual sphere is utilised. This sphere is projected on the P-facet element at the contact point with another body to calculate the resulting forces. These forces and moments are then lumped onto the nodes corresponding the the point of interaction on the body. The orientation and position of the element is then updated according to change in velocities resulting from the given loads.

When not using planar P-facet area elements, contact detection is achieved in an equivalent manner with the cylinder elements.

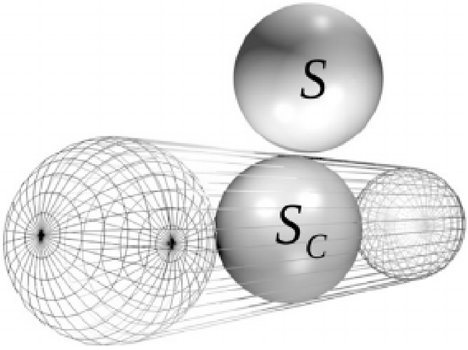

Figure 2.2: Interaction between a cylindrical connection and a sphere using a virtual sphere (Effeindzourou et al., 2016).

Grid nodes only interact with other grid nodes through the cylinder elements. They do not interact with other bodies. Each element keeps track of all connected elements and in order to deactivate interaction between adjacent elements. This way, dense grids with adjacent cylinders overlapping can be generated.

Two material models and the accompanying contact formulations are used in simulating the flexible elements. For internal interactions in the grid, elongation of the cylinders for example, the "CohFrictMat" model is used. This enables the grids to have a tensile capacity. The standard "FrictMat" model is used for external interactions.

The stiffness used to calculate internal forces and moments acting in the elements are given as:

$$k_n = \frac{E_c \pi r_c^2}{L_c} \tag{2.8}$$

$$k_s = \frac{12 E_c \frac{\pi r_c^4}{4}}{L_c} \tag{2.9}$$

$$k_b = \frac{E_c \frac{\pi r_c^4}{4}}{L_c} \tag{2.10}$$

$$k_t = \frac{G_c \frac{\pi r_c^4}{2}}{L_c} \tag{2.11}$$

where k_n, k_s, k_b and k_t are the normal, tangential, bending and torsional stiffness respectively. E_c is the young parameter of the connection, r_c the radius, L_c the length and G_c the shear modulus. When disabling rotational resistance in the nodes, only the normal stiffness k_n is active.

2.2.3 Grain geometry

Macroscopic friction angle is closely linked to grain geometry, and some studies suggest for simulating soil behaviour with friction angles above 22 degrees more complex geometries than simple spheres are necessary or the implementation of rolling resistance (Chareyre, 2007).

Real grain geometries vary significantly and may have a large degree of angularity and irregularity. To be able to emulate this quality there are mainly three methods in use:

- The use of clumps of spheres to form complex geometries of grains
- The use of an applied rolling resistance between spheres
- The use of polyhedra to achieve angular shapes at low computational cost

Grain roughness increase through the use of clumps will be the focus of this thesis.

Particle clumps

A study published in 2012 (Kozicki et al., 2012) shows the effect of varying grain geometry in a simuated triaxial test by use of Yade, In this test, the geometry of the grains is modelled as clusters of spheres fused together as one to imitate irregular grain geometry of real soils. This analysis varied the input from the simplest spheres to disc shaped clusters of more than 40 clumped spheres. A cubic sample of 10x10x10cm^3 was generated in the simulation consisting of 594,500 spheres in total for the most complex grain geometries.

The sample was generated by randomly placing particles with linear grain size distribution ranging from 2.5mm to 7.5mm in diameter into the cubic container without the effect of gravity. The specified porosity and volumetric weight of the experiment Karlsruhe sand was obtained through iteration by varying the internal friction angle μ from 0 to 30° until the desired configuration was obtained. Then dynamic compaction was used to prestress the material to the target stress which led to a random reordering of grains in the sample. Kinetic energy was monitored and allowed to subside before adjusting the internal friction angle, μ, to 30° as given for the real sand. As expected, the rougher particles exhibit higher frictional angles and thus higher mobilized strength as well as increased dilatancy. This can be explained by their increased rolling resistance.

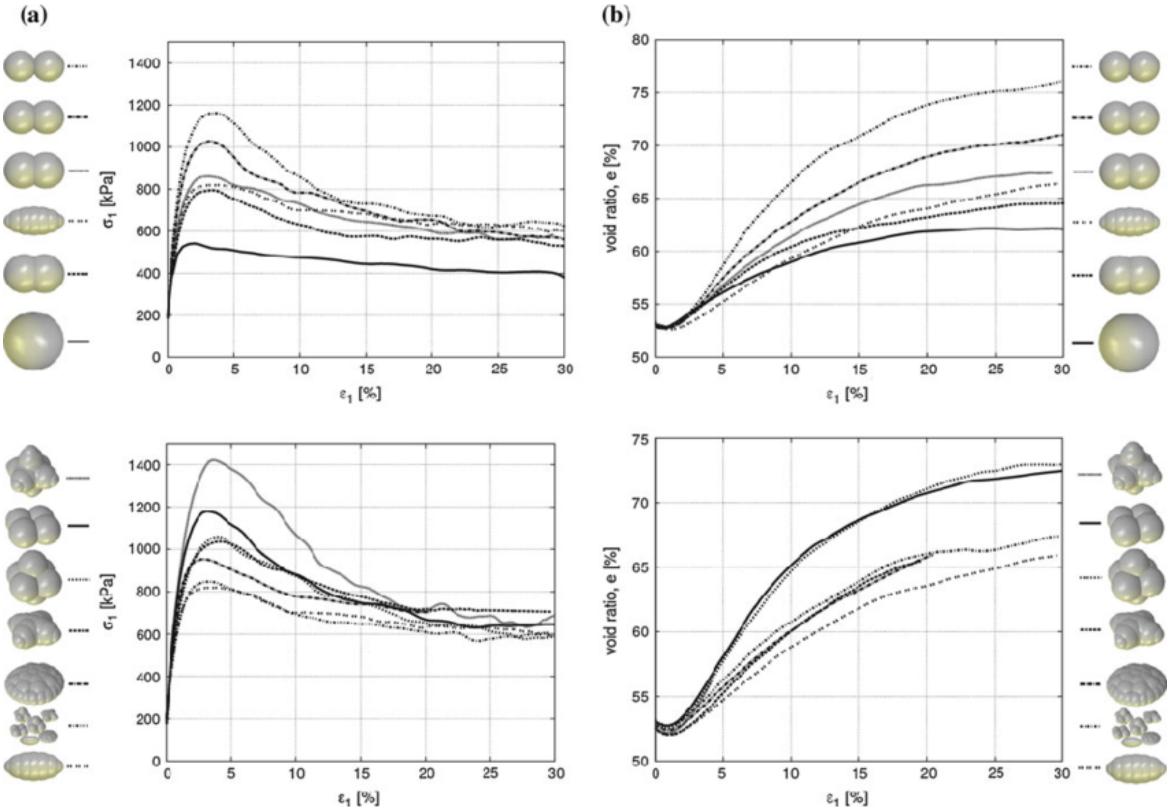

Figure 2.3: Varying grain roughness through the use of sphere clumps. Samples isotropically compacted to 200kPa. From (Kozicki et al., 2012).

Figure 2.3 shows that a large frictional capacity can be reached with a simple cluster geometry consisting of only two spheres, which reached a peak principal stress of almost 1200 kPa, only surpassed by the much more complicated geometry of the grain exhibiting the highest strength. The two-sphere clump also exhibited more than twice the peak principal stress of the single sphere. The overlap of the two spheres also has a significant effect on the macroscopic behaviour. As can be expected, a cluster with a length of two sphere diameters gives the largest roughness of the configurations. By varying the distance between the spheres the roughness can be calibrated from the maximum down to the friction of a single sphere, making it a simple and flexible tool for parameter calibration of peak strength.

For all different cluster shapes the samples reached critical state at large strains at principal stress of similar magnitudes of between 600-700 kPa at 30% vertical strain. The peak stress is therefore more heavily influenced by starting porosity for the rougher particles.

At critical state the grain roughness also influences the energy distribution. As the samples dilate, the number of contact points as well as the normal contact forces are decreased. Normal forces encompass a large degree of elastic forces and thus kinectic energy is increased as a consequence of the release of elastic energy when dilation occurs. With the rougher grains this effect is larger due to increased dilation (Kozicki et al., 2012).

2.2.4 Scaling and rate effects on results

Density Scaling
As shown above, the critical timestep is implemented as a function of the square root of particle density over E-modulus to ensure adequate precision when updating interactions and integrating motions. For large stiffness moduli and low density, this leads to long calculation times and the simulations show instabilities due to sudden large accelerations of particles when releasing elastic energy. Naturally, fewer particles in the sample accentuate these effects.

To accelerate and stabilize the simulations, a density scaling of the soil material can be used. This allows for higher stability through increased inertia when elastic energy is released and particles rearranged.
By increasing the density by a factor of ten the timestep is increased by $\sqrt{10}$, effectively reducing the computation time by two thirds if all else is equal.

An article published in geotechnique in 2000 utilised a density scaling of 10^{12} coupled with a strain rate of 10^{-5} and no numerical damping, deeming it as to have negligible effect on the quasi-static behaviour(Thornton, 2000).

Research of parameter calibration published in 2008 found that density scaling of factors of 10^4 and 10^8 without damping influenced the DEM results. The factor of 10^4 had a minor effect on the peak stress, and a larger impact on the post peak response. At a scaling factor of 10^8 the results were majorly distorted (Tu & Andrade, 2008).

Density scaling is a contested topic in the literature. It is yet unclear as to what impact density scaling has on the results when using lower, more reasonable scaling factors that still have the potential for substantial reduction of computation time.

Damping and rate effects

Non-viscous damping gives a dependency of the observed peak stress in the generated triaxial tests to the strain rate. Chareyre (2007) shows that peak stress increase is proportional to the damping coefficient at a constant strain rate. This underlines the fact that DEM are built on the laws of dynamics and as such dynamic effects have to be taken into consideration when setting out to simulate quasi-static tests such as triaxial tests. However the study also claims that a strain rate of 0.01/s with a damping coefficient of 30% is sufficient in minimizing the impact of dynamics. Figure 2.4 shows that the impact of strain rates on peak stress is negated with strain rates of the order of magnitude of 0.01/s. This highlights however, that the influence of damping, density and strain rate has to be evaluated carefully for any given simulation.

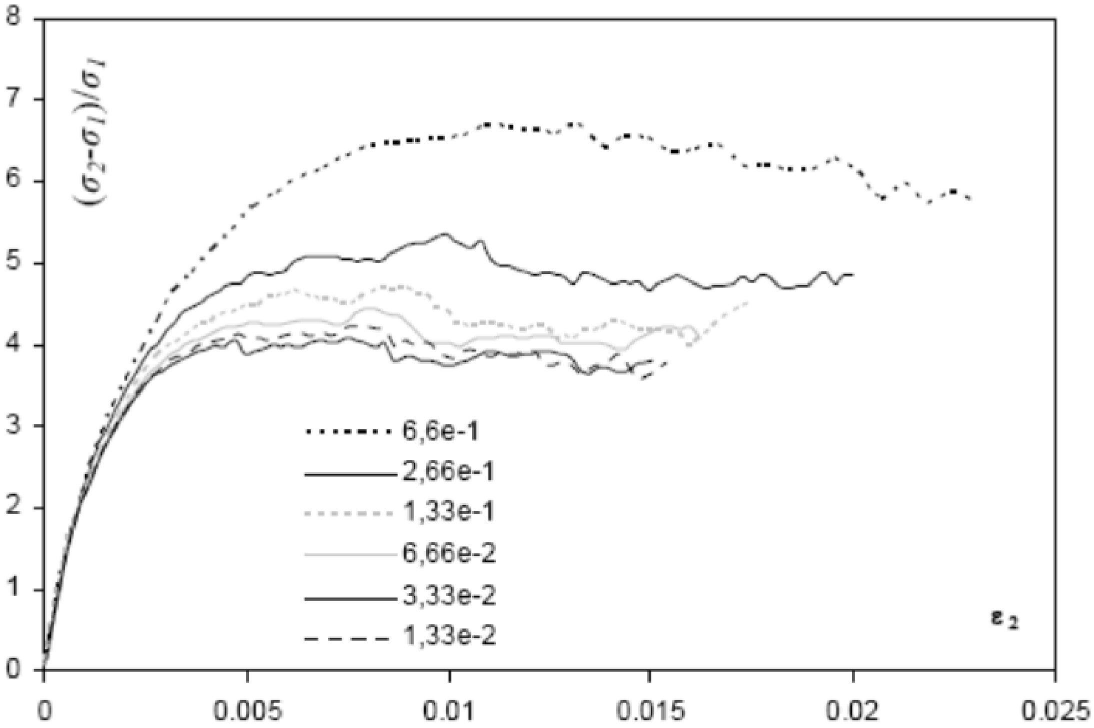

Figure 2.4: Effect of strain rate on stress-strain curves. From Chareyre (2007).

Particle count

In triaxial experiments conducted by Chareyre (2007) the statistical consistency of results where as expected closely linked to the number of particles in the sample. The statistical variation decreases substantially from 500 to 4000 grains, and at 8,000 particles the deviation in results is 2.3% on stress values for the given simulation setup. Other papers also report that a particle count of 8,000 gives consistent macroscopic behaviour (Salot et al., 2009).

2.2.5 Shear localisation

Shear localisation is a result of sudden loss of material stability, going from uniform deformation of a material, to highly localised strains. In the following section, characteristics of shear band formation and related phenomena described in the literature will be presented. The presented observations were made employing both numerical simulations and empirical methods.

Characteristics
It is typical to differentiate between two types of shear bands. Persistent shear bands, which exist over large strain intervals, and temporary shear bands. Persistent shear bands are commonly what is observed in lab experiments and at soil failure. Temporary bands typically appear before and during persistent shear band formation and is not readily visible with the naked eye (Kuhn, 2017).

Shear band formation occurs when around the peak stress, then the stress typically drops down to a residual level as the material fails (Iwashita & Oda, 1998).

In looser material and at low strain rates, the shear band formation normally occurs well into the post-peak region (Iskander et al., 2015).

Oda and Kazama (1998) made two important observations about shear bands:

1. The material accumulates shear strain distortion and form large voids inside the shear band zone.
2. Strongly localised rotations are also observed along the shear band boundaries.

These observations are related to the instability of force columns in the material. Iwashita and Oda (1998) concludes that the development of force chains occurs for both samples with and without rolling resistance in the strain hardening process. The buckling of these columns occur simultaneously as the shear bands are developed. They argue that the large local porosity increase and rotations in the shear band are the result of the column buckling. When the columns topple over, the particles rotate with the columns. Through interlocking particle geometry and rotational resistance in particle contacts, the rotation is transmitted to surrounding particles, also forcing dilation through the particle rotations.

Buckling of columns is accelerated by the loss of local contact number resulting from large localised dilation in the bands (Oda et al., 1982). The columns become more susceptible to buckling due to the opening of the soil structure, decreasing lateral support.

Oda and Kazama (1998) reports that it is necessary with a dense enough material to create force columns prone to buckling. The soil density is closely related to contact number and shear bands cannot form in loose samples due to no formation of straight, strong vertical columns that can buckle. In a loose material the force columns are not formed straight enough, leading to premature, more evenly distributed failure before loading the columns to the critical levels required for shear banding. It is also suggested that peak stress increases with increased mean stress, due to increased lateral support of said columns.

Kuhn (2017) suggests that tracking the average number of contacts in a sample can be misleading, as a number of the particles in samples not subjected to gravitation is not actually contributing to the force networks, even though being in contact with other particles.

Bardet and Proubet (1991) claim that the shear band thickness is about 8-10 times the mean grain diameter of the sample.

Oda and Kazama (1998) also report the shear band thickness to be around 8 times the mean grain diameter and that DEM papers reporting thickness of 15-20 mean grain diameters have neglected the contribution of rotational resistance. It is also noted that the thickness might vary somewhat along the curved shear band. The bands are also known to increase in thickness at higher strain rates (Iskander et al., 2015).

Development of multiple bands

Multiple, intersecting shear bands can form during localisation. 2D DEM planar compression test performed by Iwashita and Oda (1998) showed diagonally crossing shear bands. The tests exhibited mainly counterclockwise rotations in one band and clockwise rotations in another. The direction of the rotations are noted to stem from the direction of buckling of the force columns.

Conventional triaxial compression tests performed by Suzuki and Yamada (2006) showed stress fluctuations with multiple local minima and maxima in the deviatoric stress development. At the first stress minimum following the stress peak, the primary shear band is fully developed. Following this phase, a new minor stress peak develops with the subsequent local stress minimum where the secondary shear band becomes visible on the sample surface (Suzuki & Yamada, 2006). This suggests certain conditions cause alternation of the localisation in primary and secondary mechanisms.

Higher magnitudes and frequency of stress fluctuations are associated with increased interparticle friction. It is also connected to increased particle rotations (Kuhn, 2017).

Boundary conditions

Most stress conditions for geotechnical problems are either plane strain or truly three dimensional with all different principal stresses (Alshibli & Sture, 2000). However, one of the most widely used laboratory test is the axisymmetrical triaxial test. For homogeneous, dense sands, planar tests show higher peak strength at lower strains than triaxial tests at the same confining stress (Marachi et al., 1981). Triaxial tests can therefore in many cases be regarded as conservative for engineering applications. However, for soils containing imperfections and irregularities, plane tests are more susceptible to failure through mechanisms of shear localisation at lower deviatoric stresses than triaxial tests (Peters et al., 1988). This questions the idea that triaxial results give conservative estimations of design parameters.

Biaxial tests are the preferred testing procedure for examining shear bands in a laboratory setting. Tests performed in plane strain condition are more susceptible to loss of stability leading to shear localisation than the conventional triaxial test. The axial symmetry of a triaxial test makes it more stable and less prone to exihibit shear banding (Alshibli & Sture, 2000).

Since the triaxial pressure cell typically has complicated the imaging process, the plane strain tests performed with transparent rigid boundaries provide greater detail of shear band development.

Plane strain mobilized friction is considerably higher and occur at lower strain than for triaxial tests. This is most notable for dense samples at low confining stress. This difference is decreasing as initial sample packing density is decreased or confining stress is increased for the tests (Marachi et al., 1981).

For triaxial compression, the shear bands become visible at considerably higher strains than at the strain corresponding to peak stress. Dilation is reduced significantly immediately before the shear bands become visible. Also, the stress and volume curves level off when the shear band is fully developed (Peters et al., 1988).

Low values of the b parameter during plane strain tests suggests that stress conditions close to plane strain can occur for triaxial compression with only a small deviation from the ideal end conditions (Peters et al., 1988).

Periodic boundaries have also been employed when studying shear banding. However, the periodic boundaries can only capture periodic phenomena with spatial periods less than the distance between the periodic boundaries. They also force phenomena of potentially infinite length such as shear banding to be oriented normally to the periodic bounds. As shear bands are not periodic phenomena and form at an angle less than 90° to the periodic boundaries, they cannot be represented correctly (Bardet & Proubet, 1991).

Orientation of bands

Shear bands in three dimensions are not flat planes, but may be slightly curved. Especially when otherwise intersecting with the top and bottom loading platens. The orientation seems to be highly sensitive to the boundary conditions, showing curvature especially in samples confined by rigid boundaries (Oda & Kazama, 1998). Loose samples are more sensitive to boundary condition than dense (Vardoulakis et al., 1978).

The initial finely dispersed temporary shear bands found at pre-peak strain levels typically show gentler inclinations than the final persistent bands (Kuhn, 2017).

Iskander et al. (2015) writes that Mohr Coulomb theory of shear band orientation predicts the manifesting band orientation closely at quasi-static strain rates, but the bands shows a steeper angle with increased strain rate.

According to Mohr-Coulomb theory, the orientation angle of the shear bands is predicted to be:

$$\theta_C = \frac{\pi}{4} + \frac{\varphi_p}{2} \tag{2.12}$$

where φ_p is the peak friction angle.

Based on the assumption that rupture surface orientation coinciding with zero extension lines, Roscoe (1970) proposed the following relation for shear band orientation:

$$\theta_R = \frac{\pi}{4} + \frac{\psi}{2} \tag{2.13}$$

where ψ is the angle of dilatancy.

Arthur et al. (1977) reported that empirical data suggests the shear band orientation to lie between the Mohr Coulomb and the Roscoe orientations. Thus, the following empirically derived relation was proposed:

$$\theta_A = \frac{\pi}{4} + \frac{\varphi_p + \psi}{4} \tag{2.14}$$

Fabric anisotropy

According to Kuhn (2017), elongated grains orient themselves with the flatter direction in the direction of the principal compression stress, and the elongated direction in the direction of extension. This is an example of increased force anisotrophy as a sample is subjected to deviatoric loading.

With gravitationally deposited particles, fabric anisotropy is normally achieved. Particles will orient themselves with the flatter direction in the direction of deposition. The longer particle axes tend to align perpendicularly to the direction of gravity. This also causes the contact normals to primarily be oriented in the direction of deposition. As samples with a larger number of grains oriented in the direction of the maximum principal stress develops stronger columns in this direction, it is expected to influence the shear band development that rely on these strong columns. Computer generated samples without gravity have a more uniform fabric orientation (Kuhn, 2017).

Tests performed by Oda (1985) have confirmed that dilation and strength are higher for samples experiencing loading in the direction of deposition.

2.3 Determining macroscopic parameters

The macroscopic E-modulus is determined from the initial maximum stiffness of the sample, and is as such representing the aggregate stiffness of the whole sample body. The initial deformation stems from the elastic compression of each particle in the assembly before particle rearrangements. It is determined as:

$$E = \frac{d\sigma}{d\epsilon} \tag{2.15}$$

Friction angle
Peak friction angle is determined at the maximum deviatoric stress. For cohesionless soils, mobilized friction angle is given as:

$$\sin\varphi = \frac{\sigma_1 - \sigma_3}{\sigma_1 + \sigma_3} = \frac{q}{q + 2\sigma_3} \tag{2.16}$$

Volumetric strain
Volumetric strain of the sample is calculated as:

$$\varepsilon_V = -\frac{de}{1 + e_0} \tag{2.17}$$

where e_0 is the initial void ratio and compressive volume strain is positive.

Angle of dilatancy
Dilation angle, ψ, is given at the point of maximum dilation occurring during shearing. Plane strain and triaxial conditions give the same expression for the angle of dilatancy (Schanz & Vermeer, 1996). In the plastic strain regime and with compressive volume strain being positive it is given as:

$$\sin\psi = -\frac{d\varepsilon_1 + d\varepsilon_3}{d\varepsilon_1 - d\varepsilon_3} = -\frac{d\varepsilon_V}{2d\varepsilon_1 - d\varepsilon_V} \tag{2.18}$$

Chapter 3

Development Process

In the following chapter the development of the flexible boundary used in this thesis will be described, including the rationale behind the choices that were made. The chapter will also describe the attempts that were later discarded due to implementation issues. Furthermore, sample preparation and key features of the scripts will be documented.

3.1 Membrane Properties

Choice of method for the flexible boundary

In a triaxial test performed in the laboratory, the function of the membrane is to isolate the internal pore pressure of the sample from influence by the surrounding water, while using the water pressure to control lateral support stress. For the purposes of these numerical simulations, the primary function of such a boundary is to allow for stress controlled lateral deformation independent of surrounding border particles.

Multiple approaches can be used for this particular purpose as discussed in section 2.2.2.

The most commonly proposed methods in the literature are:

1. Membranes consisting of connected spherical particles
2. Border particle identification and force application algorithms
3. Membrane mesh consisting of flexible elements

The first option uses a simulated membrane with the use of connected spheres along the borders, with no moment resistance and applied lumped load at the particles. This approach utilises the already implemented contact detection for sphere-sphere contact but has some limitations. Because the sample is contained by the sphere bodies, the structure has to remain dense throughout the simulations to ensure no spheres escape the sample. The compressive and tensile stiffness of the connections between spheres must therefore be relatively high, reducing the geometric flexibility of the membrane. The number of particles in the membrane is also suspected to be substantial to ensure both flexibility and confinement. This in turn may impact the computation time considerably.

The second proposed approach is the use of force application on border particles of the sample. This method prohibits any effects of the membrane properties influencing the simulation results as it renders the particles completely free to deform independently of each other. It is however, difficult to implement correctly as it requires precise load lumping of stress acting on the sample surface and identification of all border particles. This approach was deemed too time consuming to implement for the scope of this project.

The third option involve flexible elements in the membrane. Yade has support for such elements, however not currently without compressive stiffness. This option was selected for assumed ease of implementation as it is using an existing feature. By using the planar P-facet triangle area elements described in section 2.2.2, sample-membrane contact detection is taken care of.

Yade also supports the use of a wire mesh model with no compressive stiffness. It is however asymmetric in the grid structure and dependant on sphere-sphere contact in the wire connections, making it close to the first option in principle. This makes it problematic in regard to contact detection and was therefore not considered as part of an effective solution.

Membrane configuration

With the cuboid sample geometry, two possible membrane configurations were considered:

- One continuous connected square membrane encompassing the sample.
- Four separate planar membranes extending outside the sample dimensions.

Initially, the simplest implementation considered was a continuous membrane with one node in each corner and finer distribution over the height to capture the variable lateral deformation. The implementations of this approach is shown in figure 3.1. This approach leveraged the fact that contact with the sample was ensured by stretching the membrane during vertical compression of the sample. This removed the need for identification of membrane nodes in contact with the particles for force application. This also allowed for easy scaling of membrane forces proportional to the change in length of the connections between nodes.

A problem associated with this approach is the uncertainty of the actual stress state of the sample due to the stiffness provided by the normally connected membranes. By connecting the membrane around the corner, an applied load in the x-direction will be resisted by the compressive stiffness in the membrane connections parallel to the x-direction. Similarly, with tensile stiffness and lateral expansion of the sample during compression, the adjacent membrane sides would provide resistance the deformation. Thus, the initial idea relied on av very low membrane stiffness to keep these effects at a negligible level. However, due to stability issues of the membrane, a larger membrane stiffness was required, rendering this solution unfeasible for use in data generation.

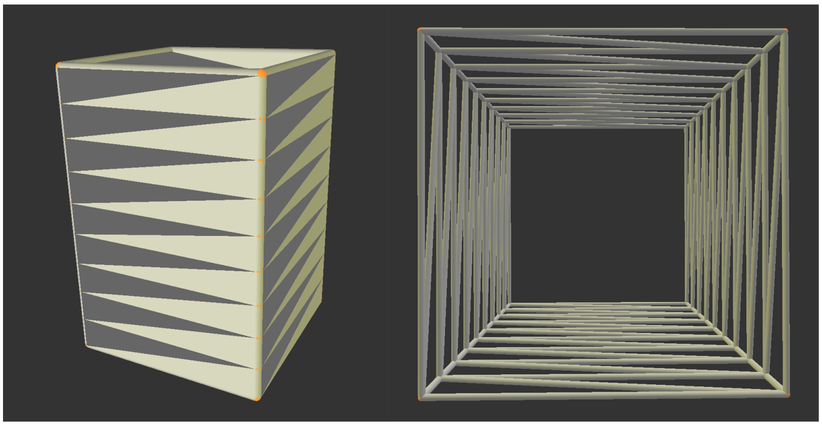

Figure 3.1: Continuous membrane. Side and top view of the membrane. Top view is rendered without area elements.

The second approach uses four separate, overlapping membranes extended outside the sample. Non-interacting material masks are used for the overlapping membranes to ensure no interaction between them, while all of them interact with the sample. The membranes are extended outside the sample to ensure full contact even at large vertical and lateral strain levels. In a lab performed triaxial test, the membrane follows the sample as it deforms vertically due to friction with the sample surface. In this simulated case this friction is set to zero, leading to frictionless sliding of the sample along the membrane surface. This is to avoid stability issues that would occur when the membrane is compressed together with the sample. This would cause overlaps of the membrane, complicating stress application and also potentially destabilizing the structure.

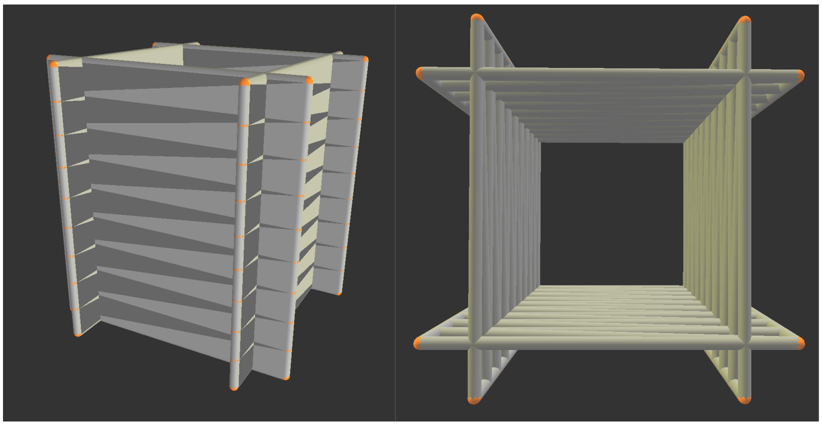

Figure 3.2: Four separate overlapping membranes. Side and top view of the membranes.

The final implementation uses multiple grid nodes over the width and height to allow flexibility in all directions. The increase in number of joints of the membrane in the horizontal direction made it necessary to identify which connections and their grid nodes are in contact with the sample. The implemented solution limits the use of membranes to just two opposing sides with rigid walls on the four others. This allows the use of the positions of the walls to identify the sections of the membrane in contact with the sample.

Membrane mesh geometry
The geometry of the membrane is determined by placing grid nodes in a specific arrangement and connecting them with cylindrical connection elements. Each group of three grid nodes is then connected to form a triangular P-facet area element.

The connections have equal tensile and compressive stiffness that can be adjusted. As the two stiffnesses are equal, it will further be referred to as membrane stiffness. It is assumed that a sufficiently low membrane stiffness will lead to the compressive capacity having minor impact on membrane geometry as most internal forces in the membrane will be tensile.

The moment resistance at the ends of the cylinder elements is disabled in this case, leaving the membrane elements free to rotate relative to each other. Thus, only the axial forces restrict the movement of the membrane.

The membrane geometry is important due to the distribution of forces throughout the structure, with both tensile and compressive forces acting. When creating the membrane mimicking boundary in Yade, a couple of different mesh structures were considered. Initially, a rudimentary triangular structure was selected for concept testing due to ease of implementation. The development of the structure is shown in figure 3.3.

While testing the prototype membrane structure it became clear that the area elements of the P-facets were too unstable to be used. The membrane would show spurious forces at reasonable time steps. It seemed to be an incompatibility of the area elements with the force applying engine in Yade, as the instability was not present when not applying lumped forces on the membrane. This limited the versatility of the membrane as the area elements had to be switched with a denser grid solely consisting of nodes and connections instead. This created a coupled problem of maintaining adequate contact detection, while keeping the membrane flexible to allow localisation of deformation in the samples.

The initial structure had some other flawed properties as well. The diagonal truss elements all provide axial stiffness in the same direction in the membrane, creating an anisotropic bending stiffness for the membrane. This may impact the data, as the membrane is more prone to deform in one direction than another.

As a solution, the diagonal connection member was removed from the grid, rendering the membrane more flexible. This however, led to the need for increased number of grid nodes to ensure sufficient contact detection. It also increased the rotational stiffness of the membrane along the borders of the sample due to the surplus membrane above and below the sample.

The final membrane design was selected to alleviate all of these issues. By offsetting every other row of grid nodes by half a connection length, a more flexible structure is achieved. This is shown as the final figure in 3.3. By distributing the axial stiffness of the diagonal elements more evenly in every direction across the membrane, the membrane is expected to deform more evenly. This offset structure provides each node with multiple axes of rotation for the surrounding elements, of which there is no rotation resistance. Thus, it increases the membrane's compliance in assuming different geometries. It also creates a denser structure for the same number of grid nodes, which entails lower computational cost while providing sufficient containment of the sample.

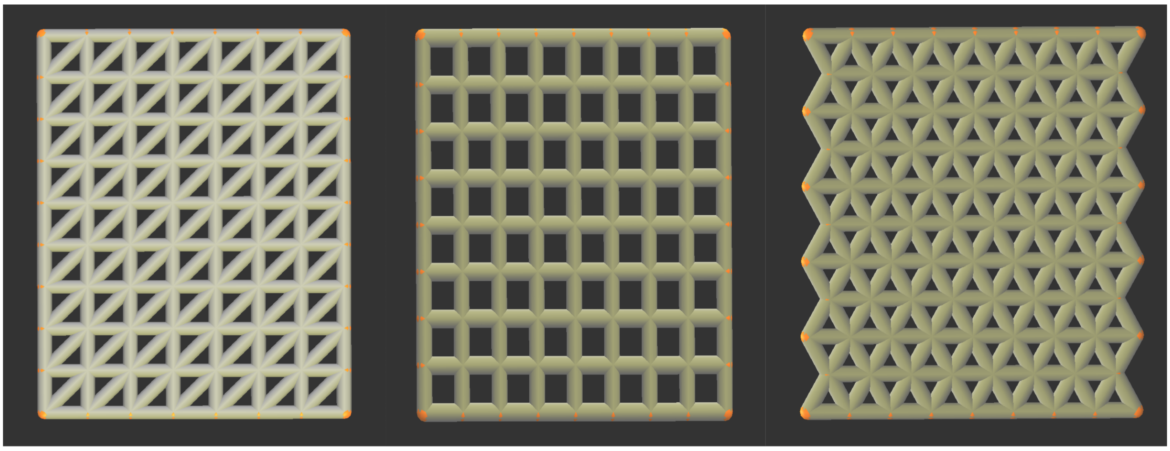

Figure 3.3: Development of membrane structure

Membrane Stability

For allowing irregular deformation over the height, a low membrane stiffness is of course beneficial. This increases membrane flexibility with the current stiffness formulations. This allows the sample to redistribute the forces internally, and limits the restriction imposed by the membrane boundary.
Contact detection for the connection grids do however require a certain membrane stiffness in order for the mesh to keep together. Thus it is a balance between the two considerations: membrane flexibility and contact detection.

The use of the membrane elements have shown to lead to spurious forces in the grids with the normal time step used with rigid boundaries in Yade. Thus, care has to be taken when selecting the time step to ensure membrane stability. The creation of spurious forces is assumed to be an artifact of the low mass of the membranes, and the close proximity of the elements in the grid. Thereby resulting in large overlaps between the membrane bodies if using a relatively large time step.

The membrane was extended outside the sample both vertically and horizontally to keep the sample contained while deforming the membrane and increasing contact area with sample.

3.2 Sample Properties

Sample Geometry
For standard laboratory performed triaxial tests, a cylindrical sample is most commonly used. This is due to its more stable nature compared to a cuboid sample which suffer from edge effects and is less suitable for cohesive materials. A consequence of this cylindrical shape is that the test can only represent conditions with stress components in the horizontal plane being equal. For many geotechnical problems such as dams, roads, fills, etc. all three of the principal stresses are normally non-identical.
In order to facilitate the use of true triaxial testing with three-dimensional anisotropic stress conditions, a cuboid sample geometry was selected. This allows for control of the six boundaries of the sample as opposed to the standard cylindrical shape.

Particle Geometry
Particle geometry is expected to be the most important parameter in determining shear banding behaviour. The simplest geometry for DEM simulations is as previously discussed the spherical shape. Individual spherical particles have very limited rotational resistance, and is assumed unable to mimick real soil behaviour in shear localisation. It is however the building block of every DEM program due to its simplicity in contact detection and generation. By rigidly connecting these singular spheres together in clumps, geometric anisotropy can be achieved. Rough, naturally occurring sand grains have a large degree of angularity which can be imitated with these clumps.

Clump templates are created by designating the relative radius and position of each sphere constituent of the agglomerate clump. This determines the geometry of the clump type. There is no hard limit on the number of spheres in each clump, but increasing complexity in the geometry entails a higher particle number and thus prolonged computation time.

Yade also has support for polyhedral particles more closely mimicking naturally occurring sand grains, but this method was deemed too computationally costly for the target number of particles necessary to examine shear localisation.

Two particles are used in the compressions tests - particle A and B shown in figure 3.4. Particle A is the simplest geometry in Yade - an individual sphere. It is included as a benchmark of limited rotational resistance from contacts with other bodies.
Particle B is an elongated clump particle consisting of two spheres. It is included as a computationally inexpensive particle of large rotational resistance and roughness.

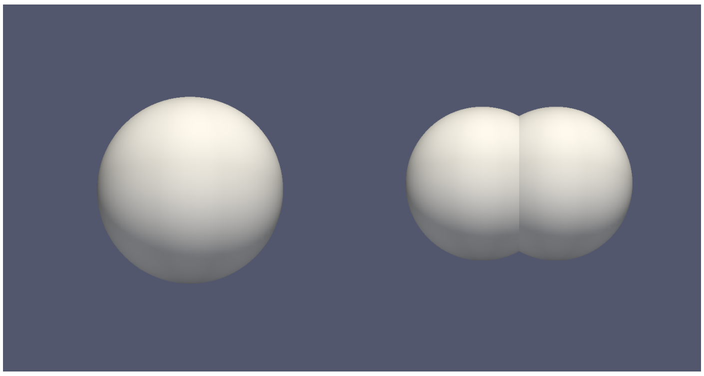

Figure 3.4: Particle A and B.

Sample preparation

Sample preparation is initialised by generating a dispersed particle cloud within the sample dimensions. At this stage, every boundary is rendered as a rigid wall to ease sample preparation and ensure a sample with regular geometry. This cloud consists only of singular spheres with random orientation and position within the specified borders. The cloud as a whole satisfy the given particle size distribution. For clump generation, the spheres are then exchanged with specified clump templates. The distribution of the different clump templates is also given as input. In this thesis the particle sizes follow a uniform distribution of particle radii. The distribution is determined by the parameters "rMean" and "rRelFuzz" in the code.

The particle radii are uniformly distributed between r_{min} and r_{max} given below:

$$r_{min} = r_{mean} \cdot (1 - rRelFuzz) \tag{3.1}$$

$$r_{max} = r_{mean} \cdot (1 + rRelFuzz) \tag{3.2}$$

When exchanging the spheres with clumps in the sample, the clumps are scaled so that the volume of the inserted clump matches the volume of the sphere it replaces.

To reach the prescribed isotropic stress, the particles are homogeneously increased in size, gradually decreasing the porosity and creating contacts between the bodies. This process of increasing particle size to increase stress is termed "internal compaction". At this stage the rigid walls are fixed in position and have zero friction for uniform compaction of the sample. Friction is then later optionally applied on the top and bottom loading platens in the deviatoric phase.

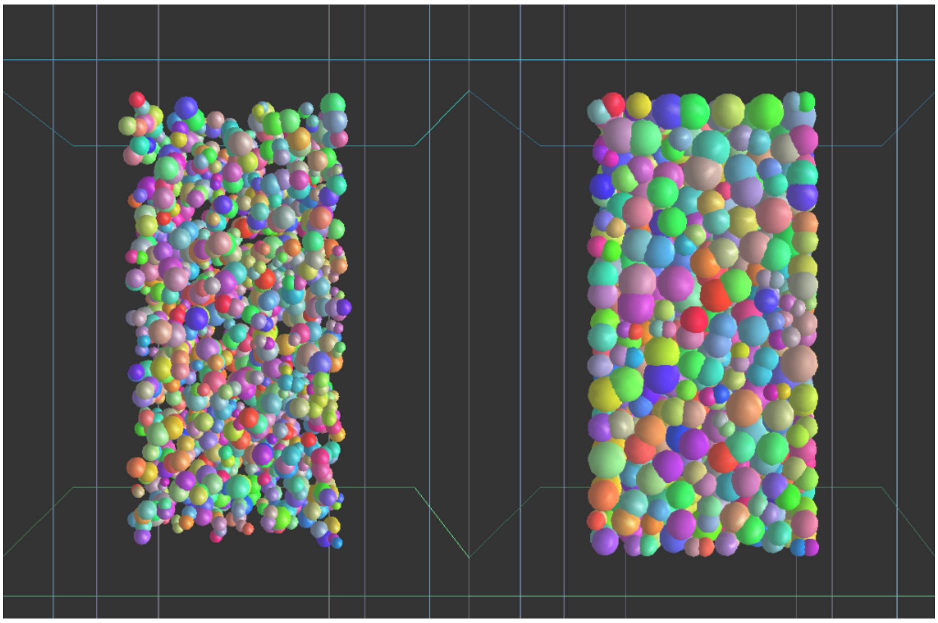

Figure 3.5: Sample preparation through internal compaction.

It is important to note that the sample preparation is conducted with no gravity acting. The sedimentation process is important for determining behaviour of naturally occurring soils as fabric is known to play an important role in the determination of material properties. In this thesis, the sample generation leads to generally uniformly distributed orientations of particles, and isotropic soil structure.

The resultant forces from each wall-sphere interaction are summed up and divided by the area bounded by the bordering walls to determine the current stress state in the sample. This stress is monitored continuously to determine when to conclude the internal compaction phase.

In combination to the stress calculation, the other variable considered as a measure of staticity is the "unbalanced forces". This is the ratio between the average resultant force on the simulated bodies and the average magnitude of interaction forces. For a simulation near complete equilibrium, the unbalanced forces should be close to zero. When the target stress is reached and the unbalanced forces are reduced to 3%, the internal compaction phase is concluded. This can be considered quite high, but as the sample also require time to settle when imported into the membrane confined cell, 3% unbalanced forces is stable enough.

For isotropic stress states, the sample is then saved for exporting into an independent simulation for conducting deviatoric compaction with either the rigid or flexible boundaries. For anisotropic stress states, the rigid boundaries are now instead slowly adjusted to reach the target stress.

For reaching a specific porosity, the REFD algorithm proposed by Tong, A.-T. et al. (2012) is utilised. The algorithm works by setting an initially high interparticle friction in the sample during internal compaction. Then, the particle friction is incrementally decreased while the confining stress is kept constant. By lowering the friction, the particles are able to gradually reach a denser configuration. This ensues until the target porosity is reached. Note that the lowest possible porosity needs to be determined at first by running sample generation at zero particle friction to find the minimum porosity.

3.3 Confining Stress on Membrane Boundaries

Multiple iterations of force application algorithms were tested. The final implementation of the membrane uses the offset triangular structure of grid nodes and connections. The rigid wall elements confining the sample in the y- and z- directions are used for identifying membrane nodes in contact with the sample, further referred to as "active" nodes. The algorithm checks the nodal position against the wall positions, and select the nodes inside the active area. Then, the active nodes are grouped into connected triangles, and the normal stress on each of these triangles are calculated depending on the area in the active zone defined by the walls.

Two solutions were developed for determining the direction of the lumped nodal forces. The first method applies the force perpendicularly to the undeformed membrane surface. The orientation does not change with the membrane deformation. This is to circumvent possible membrane instabilities that would otherwise change the direction of the membrane forces. This method uses the projected lengths of the triangle sides on the y-z-plane to determine the active area from the cross products of the projected vectors. The force is then calculated as the prescribed stress multiplied with the projected area. The lumped forces are then applied evenly at each grid node of the evaluated triangle. This even application of forces is of course a simplification to reduce computation time, but influence on membrane behaviour is negligible with a large number of nodes in the mesh.

The second approach calculated the forces acting perpendicularly to the active areas of the membrane as it deforms. It did however lead to unexpected kinks in the membrane resulting in the membrane not deforming in continuous contact with the sample. The first method is therefore used in all tests.

Cover facets
To simplify the load lumping process, what the author chose to label as "cover facets" were added. These facets work to stabilize the membrane structure by following the rigid wall as the sample deforms. The cover facets block the membrane that should not exert force on the sample. The covers are used on all borders of the sample and are controlled with the connected rigid boundary. They are shown in orange in figure 3.6.

The covers were predominantly used for the prior confining stress algorithm, but are included to allow small discrepancies in applied force to not increase sample stress on the borders. They are also used to inhibit the membrane from sliding off the sample due to the frictionless contact.

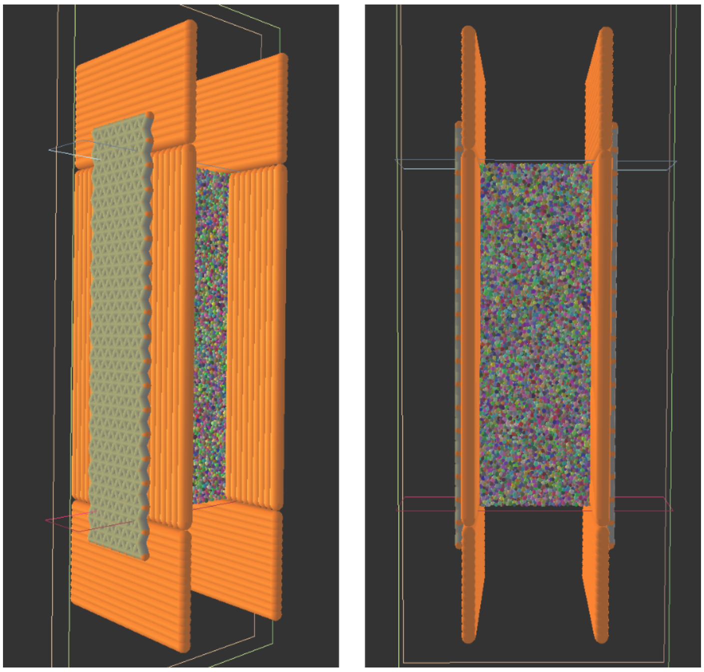

Figure 3.6: Final simulation setup.

3.4 Strain Control of Boundaries

An algorithm to control the movement of the rigid plates on the top, bottom and two of the sides of the sample was developed. Due to the irregular nature of the membrane, there was not done any attempt at calculating the average strain across the membrane borders for use in the stress calculation. Therefore the generated stress plots will show engineering stress curves. Vertical strain is factored in for the lateral stress calculations of the rigid walls.

All lateral rigid walls are individually controlled depending on the measured stress acting on them. The walls are adjusted by changing their velocity depending on the difference in measured and target stress. The wall velocity is given as a fraction of the set vertical strain rate. It is given as:

$$(1 - abs(stress/targetStress)) \cdot controlVelocity \tag{3.3}$$

where controlVelocity is dependant on the volume change potential of each boundary. Illustrated as:

$$controlVelocityX = widthX/(widthX + widthY + height) \cdot 10 \tag{3.4}$$

3.5 Data Evaluation

A number of different methods to extract useful data from the simulations were employed. Most of these methods use the visualisation program Paraview to render the captured information in post processing. The required data is exported from Yade per particle using the builtin "VTKExporter" module at set strain levels. The data was captured at each 0.25% of vertical strain to render the development as the samples were exposed to deviatoric loading. The data evaluation methods are listed and further explained below:

- Force chains
- Local and global porosity measurements
- Incremental and accumulated rotation of particles
- Stress measurement on rigid boundaries
- Tessellated stress and strain fields
- Particle displacement pathlines
- Contact number tracking

Force chains
The force chains render the interaction forces graphically in order to visually determine different force networks through the sample. How the sample is carrying the load from the top to the bottom load plate is expected to change with increasing shear localisation and is therefore of interest. It is also known that soil loads are not distributed evenly across the sample as for a material continuum, but instead localised through select strong columns in the material. These columns are subjected to large compressive forces and prone to buckling. By visualizing the force columns, one can observe the column buckling associated with shear localisation. The force chain figures display the chains as tubes of radius and color corresponding to the normal force acting between the particles.

Porosity measures
Porosity changes during simulation are of interest in determining soil behaviour. Global porosity measurements can indicate when critical state behaviour occurs, and graphical renditions of local porosity can reveal shear banding at the early stages of formation. Porosity changes of the sample are expected to be largely uniform across a homogeneous sample until shear localisation occurs. At this point the rotation of the particles in the shear band region is expected to increase local porosity.

The global porosity measurement is performed through the integrated Yade function "voxelPorosity". This is using a conceptually simple approach to calculate the porosity of a given volume in the sample at a specified resolution. The volume is partitioned into a large number of small cubes corresponding to the given resolution in three dimensions. Each of the cubes internal to any particle is then counted. By dividing the number of cubes external to any particles over the number of cubes inside particles, a porosity value is determined. Evidently, a finer voxel resolution is required for finer particle sizes, leading to increased computation time.

The voxelPorosity function can also be used for determining localised porosity by using the function call on designated parts of the volume at a time.

A simple local porosity script was developed, dividing the center strip of the sample into a grid mesh of checked volumes. This method was deemed to imprecise to be used with the flexible boundaries as the sample deformation was highly irregular at large vertical strain. The local porosity measures were not accounting properly for the lateral deformation of part of the sample.

Particle rotations

Tracking incremented rotation of particles allows the graphical representation to show areas of excessive rotation. This is expected to coincide with the shear banding region, thus making it a valuable diagnostic tool for evaluating sample behaviour and visually presenting shear bands.

For each particle there is a reference orientation saved in the simulation. Rotation from this reference orientation is measured as a vector with rotations about the global axes for a given particle. This rotation vector can represent the rotation up or down to 2π then resets to zero. In order to circumvent the issue with rotations resetting when passing 2π, the reference orientation of the particles is reset at each checked strain increment. At tracking strain intervalls of 0.25% strain the rotations of particles are expected to not exceed 2π.

To account for all rotations in general with no emphasis on rotational axis in the three dimensional simulations, the visualizations are based on vector length of these rotation vectors. This is meant to be used as a measure of relative rotation, and is not applicable for determining absolute rotation in degrees.

Two different methods of the rotation tracking is used. Accumulated rotation and incremental rotation. Accumulated rotation tracking is used for clearly visualizing the persistent shear bands as they develop over large strain intervals, while the incremental rotation tracking can show temporary localised rotations as well. The incremental rotations show rotation occurring in-between each strain interval of 0.25% and is reset at each step.

Stress and strain calculation

Stress is calculated from the resultant forces of all rigid wall-sphere interactions divided by the sample area. Due to the variable deformation along the membrane border, the original undeformed area is used instead. This is then used to produce engineering stress graphs versus vertical strain. The vertical strain is however accounted for in the stress calculation.

Microstrain of tessellated volume

Tessellation of the sample involves dividing each sphere into a polygonal subdomain bounded by the surrounding particles. This results in a continuum mesh of the sample. This mesh can be used to track micro strains and stresses throughout the sample to identify localisations. Yade does provide tessellations when used together with all-encompassing rigid walls. Attempts were made to utilise the existing tessellation functions, but issues regarding the identification of the membrane as a boundary for were the tessellation were to end made it unfeasible for practical applications.

Contact number

Per particle contact number reveals local areas of dilation and contraction as the contact number is decreasing in dilatant areas where the voids between the particles increase.

Two measures are tracked for the particles: Change in contact number from initial stable state, and incremental change in contact number for highlighting changes occuring between each 0.25% vertical strain step.

As contact number and local porosity is closely related, the figures presented in this thesis showing contact number are produced from a central slice of the sample in question. This allows for visualizing the growth of large voids in the shear band.

Particle pathlines

Tracked particle displacements are visualized to show the particle paths during the formation of plastic mechanisms. This often makes it possible to visually determine the orientation of the shear bands as the material external to localisations behave as coherent blocks in translational motion.

Chapter 4

Parameter calibration

The following tests were run for the purposes of both parameter calibration for the shear localisations tests and also for comparing rigid and flexible boundary conditions during triaxial testing. The primary parameters of interest were: strain rate, damping ratio, particle normal stiffness and interparticle friction.

4.1 Method

All calibration tests were run with samples of 8,300 particles. Sample dimensions are 10 cm x 10 cm x 20 cm with triaxial strain conditions.

Generated loose cloud of mean grain radius 2.2mm. Internal compaction to 200kPa isotropic stress resulting in grain radius increase of 44% for particle A and 43% for particle B resulting in mean radius of 3.2mm. Particle radii uniformly distributed between 1.9mm and 4.5mm. Initial porosity of 37.0% and 42.8% for densest and loosest samples of particle A. For particle B the initial porosities were 31.6% and 40.9%.

Particle A was used for the calibration of strain rate, damping ratio and normal stiffness. They were performed with the densest sample configuration.

The interparticle friction tests were run with samples of particle B in order to calibrate the internal friction angle with regards to the shear localisation tests. They were performed with the densest sample configuration.

The z direction is referred to as the vertical direction and x- and y-directions as lateral. When using membrane boundaries they are applied in the x-directions of the samples, while the sample is confined in the y-directions by rigid walls.

Volumetric expansion is given as positive in the strain plots.

Sample porosity is changing with changing normal stiffness at the same mean stress. Therefore, tests were performed both on samples of densest configuration, and of equal porosity. Individual sample generation was run for all tests, but with the same initial generated particle positions and orientations in the cloud. The REFD algorithm is used to achieve equal porosity in the samples.

Four sets of simulations were run. Both rough and frictionless end conditions for the triaxial tests with rigid and flexible boundaries.

The time step is determined by the wave propagation speed in the material when using rigid walls. It is given by equation 2.6. It is set to 6e-7 sec when using flexible boundaries for ensuring stable membrane behaviour..

The default parameters used are given in table 4.1.

Table 4.1: Static parameters for calibration tests.

Input parameters	**Value**
Solid density [kg/m^3]	2800
Young [MPa]	200
Poisson	0.3
Mean grain diameter [mm]	2.2
Compaction friction [°]	0-30
Internal friction [°]	30
Isotropic stress [kPa]	200
Damping [%]	3
Strain rate [%/sec]	50

4.2 Results

4.2.1 Strain rate

Strain rate influences the measure peak stress and plastic strains. By not allowing the particles the necessary time to rearrange, a higher peak stress is measured. The strain rate of 50%/sec show satisfactorily similar stress-strain behaviour as at 2.5%/sec for the purposes of this study.

The test results exhibit large stress fluctuations with the flexible boundaries. These are assumed to stem primarily from the small number of particles in the tests. Due to very long calculation times at low strain rates, a relatively small number of particles were used.

When measuring force on top and bottom load plates, it is shown that there is a discrepancy between top and bottom stress for higher strain rates when only lowering the top load plate. The effect is amplified with increasing particle density, as with density scaling. This is occurring with zero friction on the lateral confining walls, so no friction on the lateral walls can account for this discrepancy. This is assumed to be an artefact of the stress-strain calculation procedure, which requires overlaps, where the the particle inertia is leading to too large overlaps with the moving load plates.

The stress of the bottom plate is seen to be lagging behind the stress of the top plate. This effect is visible at the highest strain rate in figure 4.1. The figures presented here do however show the average stress of top and bot measurements.

By straining with both the bottom and top loading plates, this effect can no longer be quantified when viewing a single test result, it is however evident when examining multiple stress paths for tests with differing strain rates.
One benefit of straining from both ends is that the individual loading platen velocity is halved, decreasing the numerical issues of artificially large overlaps and leading to a smoother stress response overall.

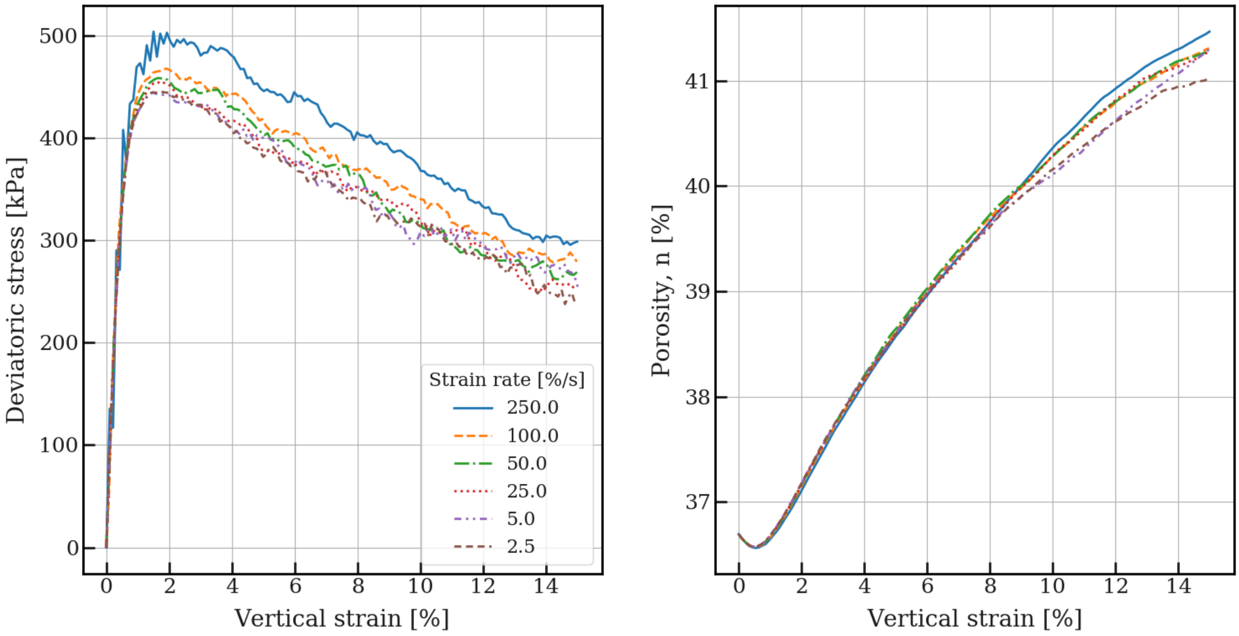

Figure 4.1: Effect of varying strain rate on sample response using rigid boundaries.

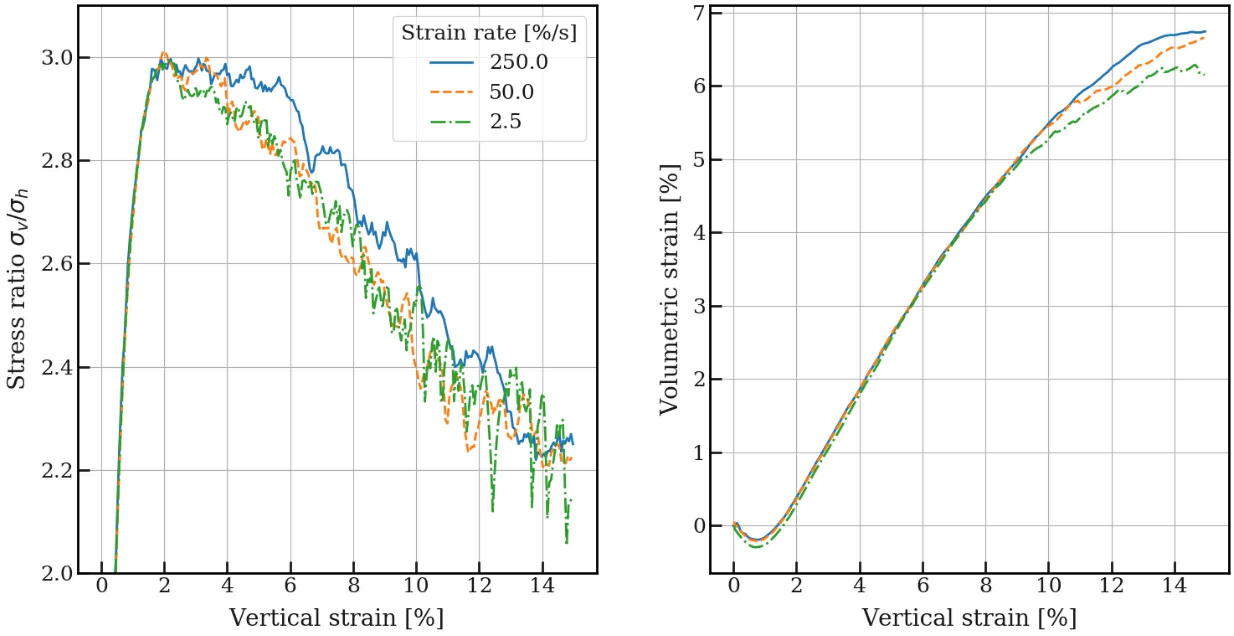

Figure 4.2: Effect of varying strain rate on sample response using flexible boundaries.

4.2.2 Damping

With the chosen loading plate velocity of 0.1m/s equalling strain of 50%/s, it was deemed necessary to evaluate strain rate effects. As previously discussed, peak stress levels become damping dependant for certain strain rates.
As shown in figures 4.3 and 4.4, the damping ratio influences the peak value and volume strain. As expected the damping ratio show larger impact on the peak stress for strain rate of 100%/s than 50%/s. Larger damping ratios lead to diminishing increases in peak stress. A relatively large stress increase occurs between zero damping and a damping ratio of 5%. In order to ensure membrane stability with sufficiently large strain rate, a damping ratio of 3% was selected.

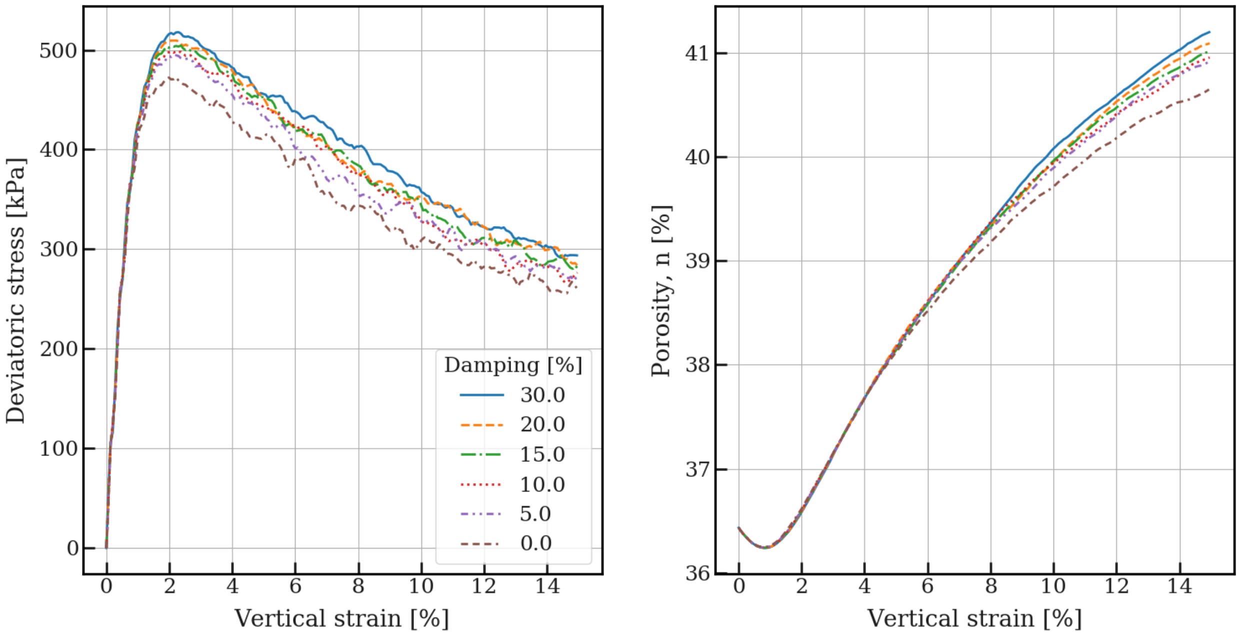

Figure 4.3: Effect of varying damping ratios at strain rate 100%/s

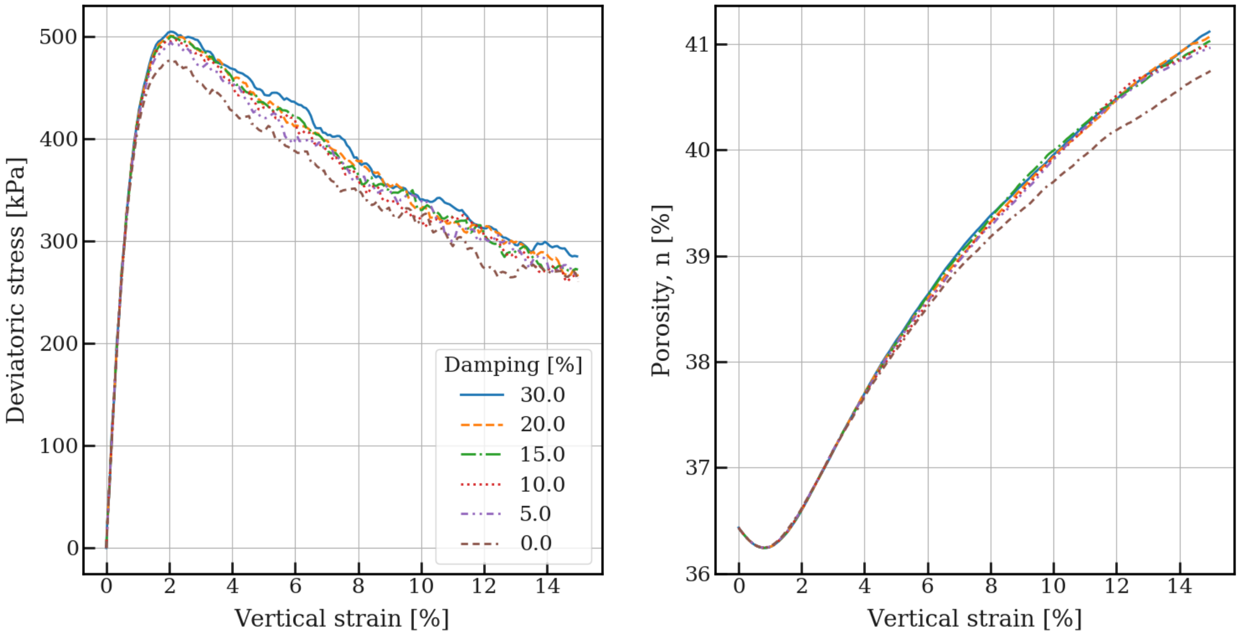

Figure 4.4: Effect of varying damping ratios at strain rate 50%/s

4.2.3 Normal stiffness

In figure 4.5 the samples show different peak values with varying interparticle normal stiffness with the same interparticle friction. This is assumed to be due to increased overlap between grains leading to denser sample configurations and thus a larger peak capacity. In order to examine this discrepancy, the samples were consolidated to the same target porosity of 40%, but as can be seen in figure 4.7 this still leads to differing stress peaks. This discrepancy is however smaller. The sample response is also stiffest for the densest packings, as is expected due to increased resistance to particle rearrangement.

The soft particle approach, simulating deformations as particle overlaps, requires sufficiently high normal stiffness to provide reasonable results. The results shown in section 4.2.3 include results of very low normal stiffness. The normal stiffness calibration tests show increased peak stress of the samples with lower stiffness. This is expected to be due to a larger average contact number in the samples resulting from large overlaps. The lower stiffness were included for comparison purposes.

The E-modulus of the samples compacted to the same porosity, show discrepancies of the lower values. This is suspected to be caused by the REFD algorithm for sample generation, where interparticle friction is gradually decreased while upholding confining stress until target porosity is achieved.

The stiffness parameters are of some uncertainty due to fluctuations of stress paths. They however show large enough discrepancy as to suggest that the response using flexible boundaries is significantly less stiff.
When comparing rough and frictionless end conditions, rigid walls show a higher sensitivity to these conditions in the macroscopic stiffness with around 15% stiffer behaviour with rough end conditions. Flexible boundaries show less discrepancy with a variation of 10%.

Rigid boundaries with rough end conditions

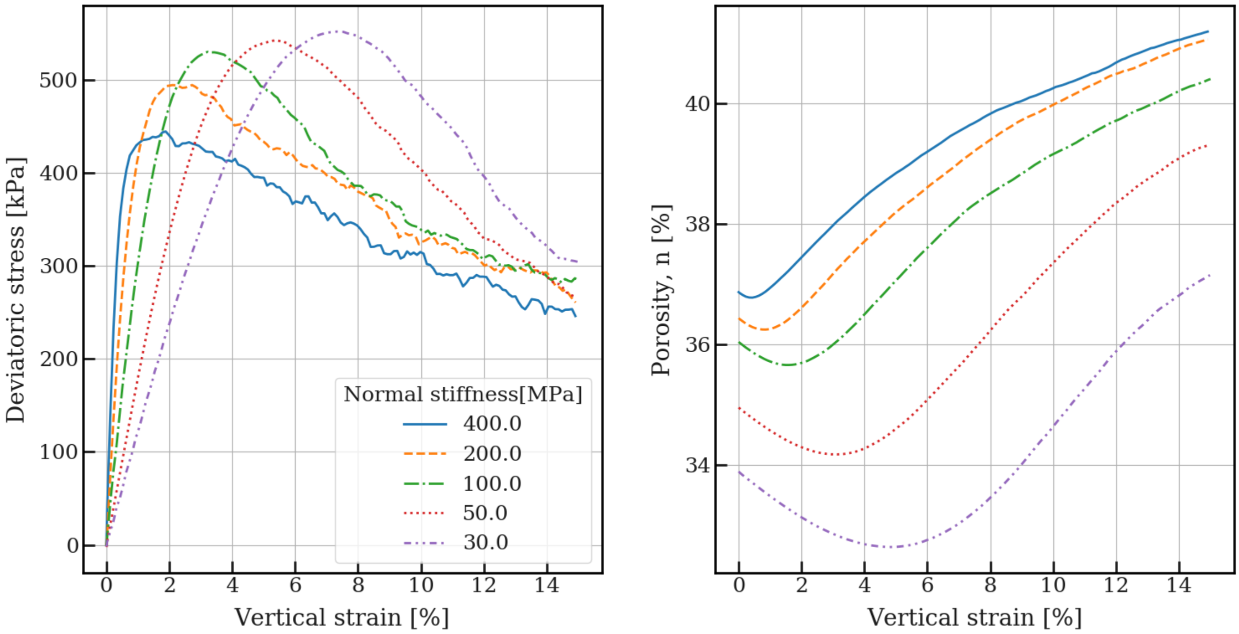

Figure 4.5: Calibration of normal stiffness parameter young - samples at densest packing.

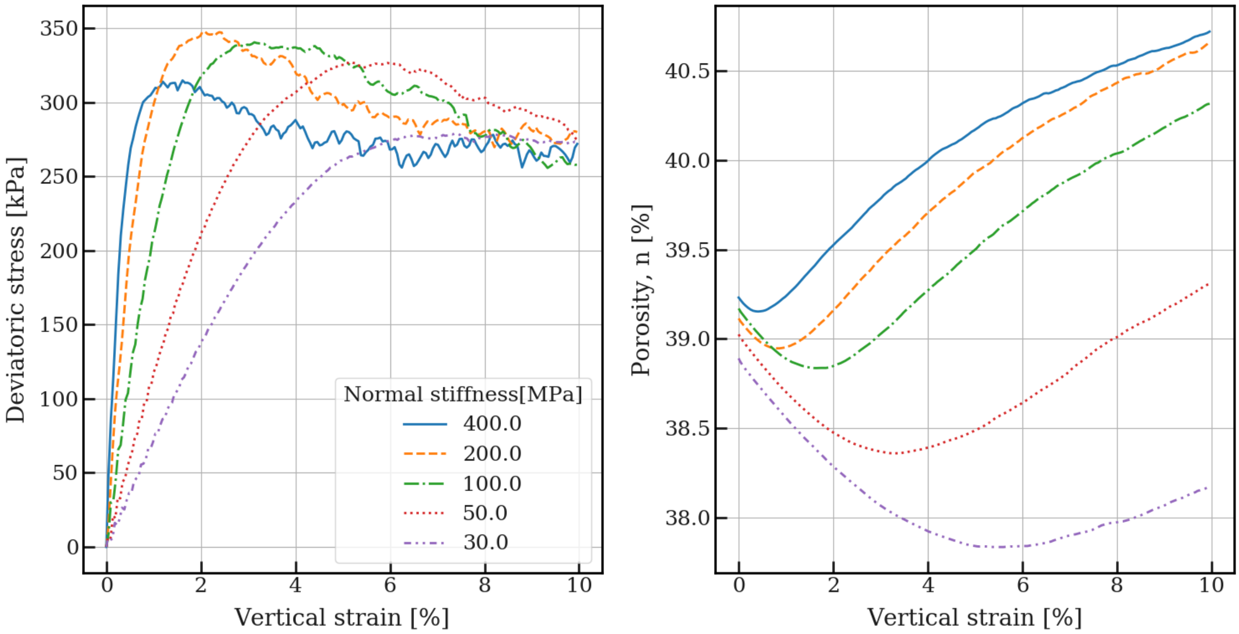

Figure 4.6: Calibration of normal stiffness parameter young - samples of equal initial porosity.

Table 4.2: Macroscopic normal stiffness for samples of equal initial porosity.

Young [MPa]	**E-modulus [MPa]**
400	101.0
200	51.2
100	24.2
50	13.2
30	8.2

Table 4.3: Macroscopic normal stiffness for samples of densest configuration.

Young [MPa]	**E-modulus [MPa]**
400	109.1
200	59.0
100	35.1
50	16.7
30	11.6

Rigid boundaries with frictionless end conditions

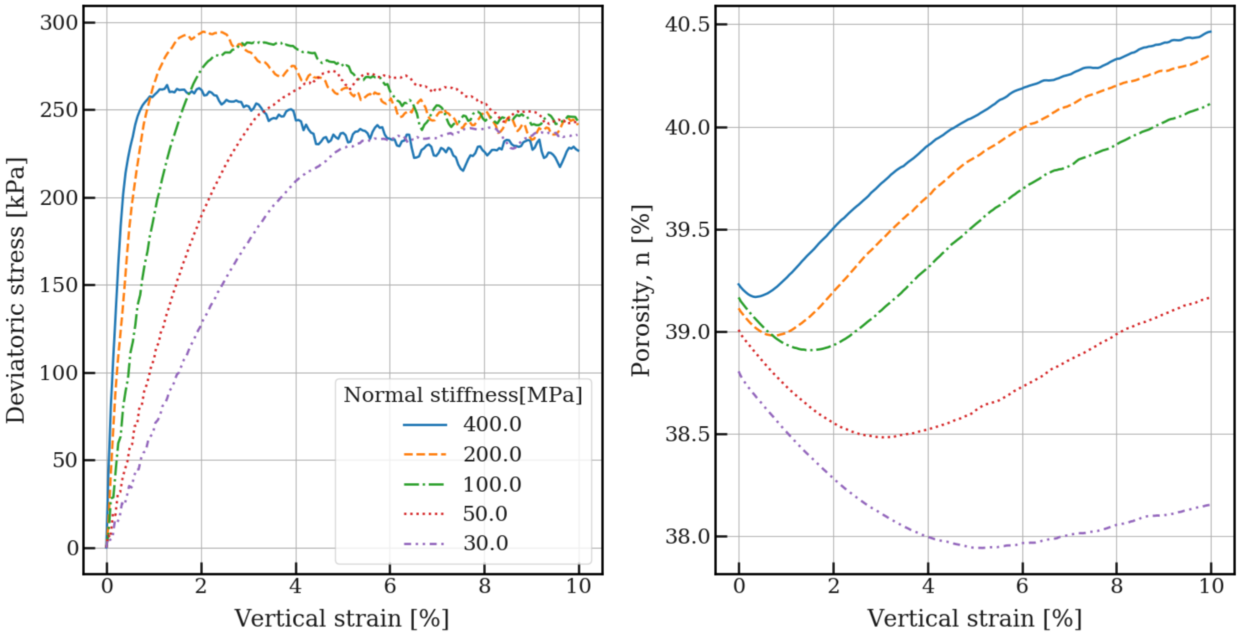

Figure 4.7: Calibration of normal stiffness parameter young - samples of equal initial porosity.

Table 4.4: Macroscopic normal stiffness for samples of equal initial porosity.

Young [MPa]	**E-modulus [MPa]**
400	89.6
200	44.1
100	22.3
50	12.6
30	8.0

Flexible boundary with rough end conditions

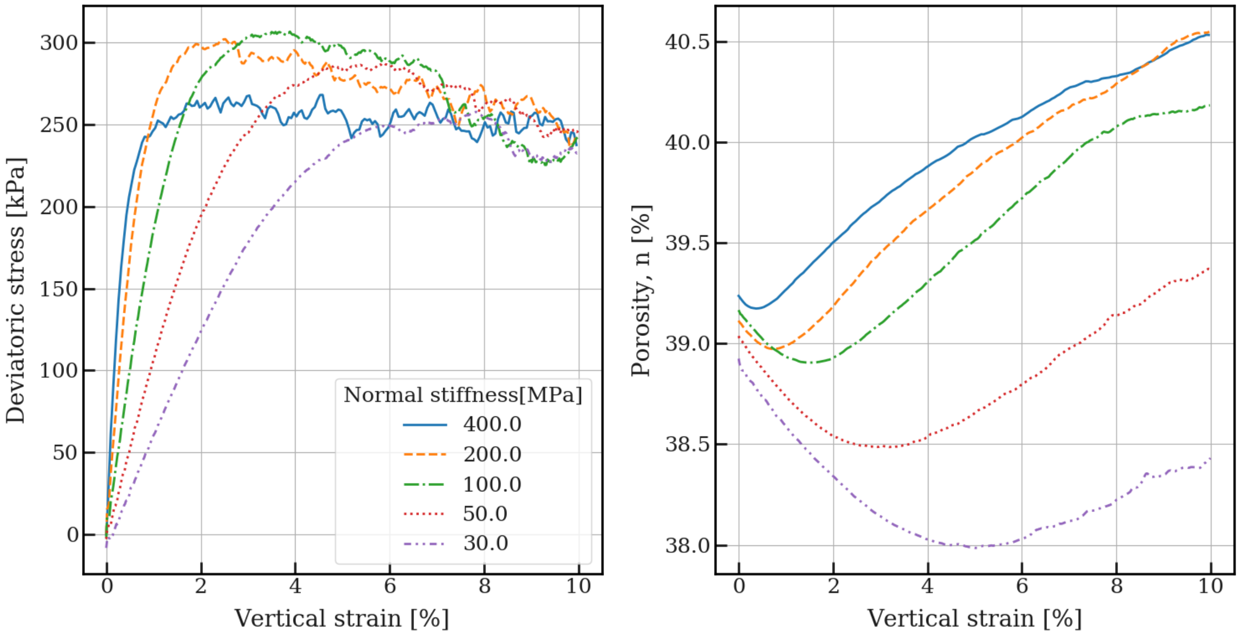

Figure 4.8: Calibration of normal stiffness parameter young with flexible boundaries. Samples of equal initial porosity.

Table 4.5: Macroscopic normal stiffness for samples of equal initial porosity.

Young [MPa]	**E-modulus [MPa]**
400	58.0
200	37.0
100	20.6
50	13.3
30	7.0

Flexible boundary with frictionless end conditions

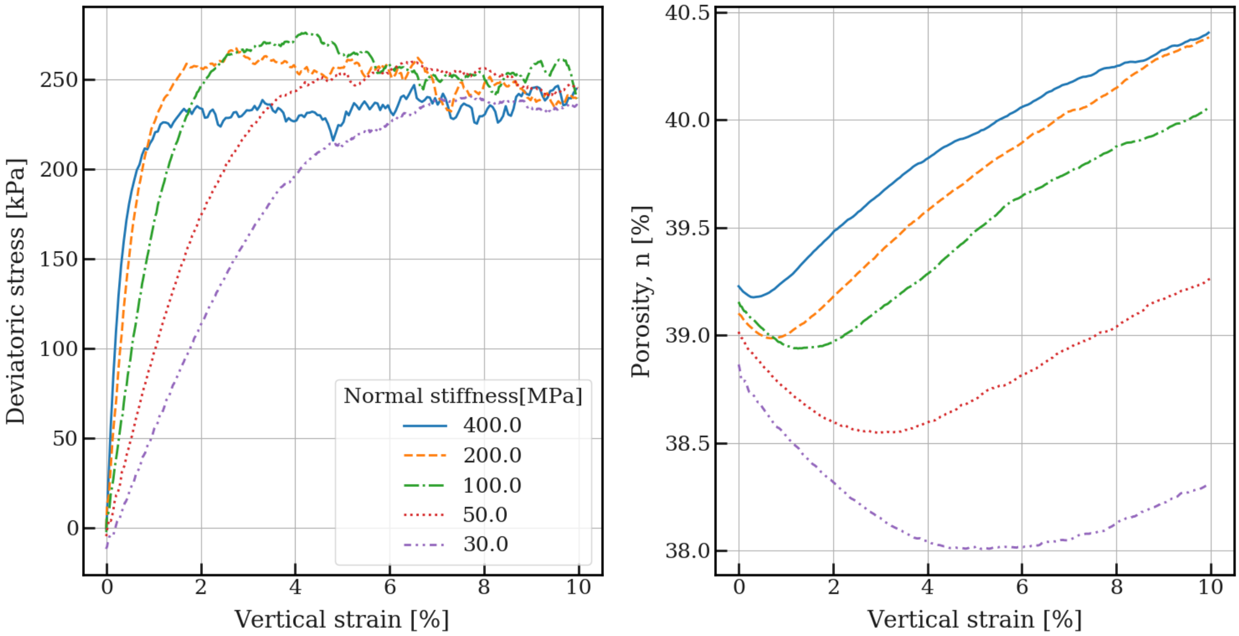

Figure 4.9: Calibration of normal stiffness parameter young with flexible boundaries. Samples of equal initial porosity.

Table 4.6: Macroscopic normal stiffness for samples of equal initial porosity. Flexible boundaries.

Young [MPa]	**E-modulus [MPa]**
400	64.0
200	39.3
100	20.3
50	12.0
30	7.2

4.2.4 Interparticle friction angle

The results are largely consistent for rigid and flexible boundaries. At interparticle friction of less than 10° the tests show no clear peak stresses. The samples exhibits primarily volumetric compaction and no dilation for zero interparticle friction.

At lower friction angles, the samples show stable dilatancy angles for large strain intervals, leading to softer, prolonged stress peaks showing less brittle behaviour. The stress peaks also occur at slightly larger vertical strain.

The tests show lower peak friction with frictionless end conditions. This is expected from Mohr Coulomb theory due to the applied shear on the sample ends rotate the principal stress directions, increasing potential maximum vertical stress.

An interparticle friction angle of 15° corresponding to measured peak friction angles between 35.5° - 38.6° was selected for use in the shear localisation tests.

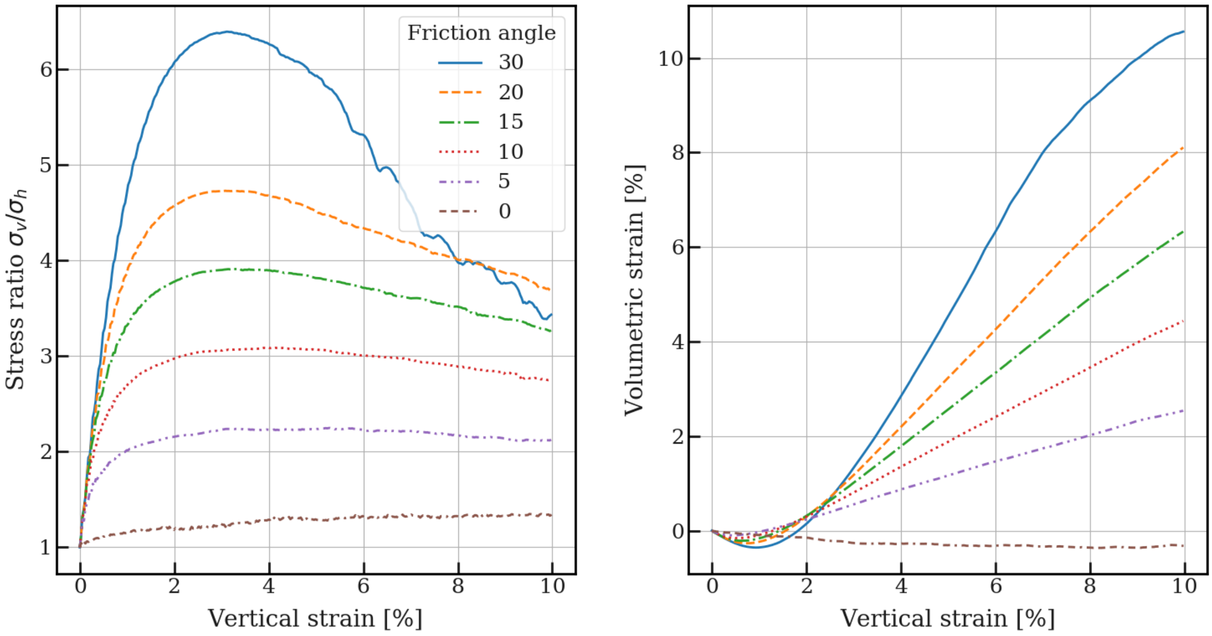

Figure 4.10: Calibration of interparticle friction using rigid wall boundaries.

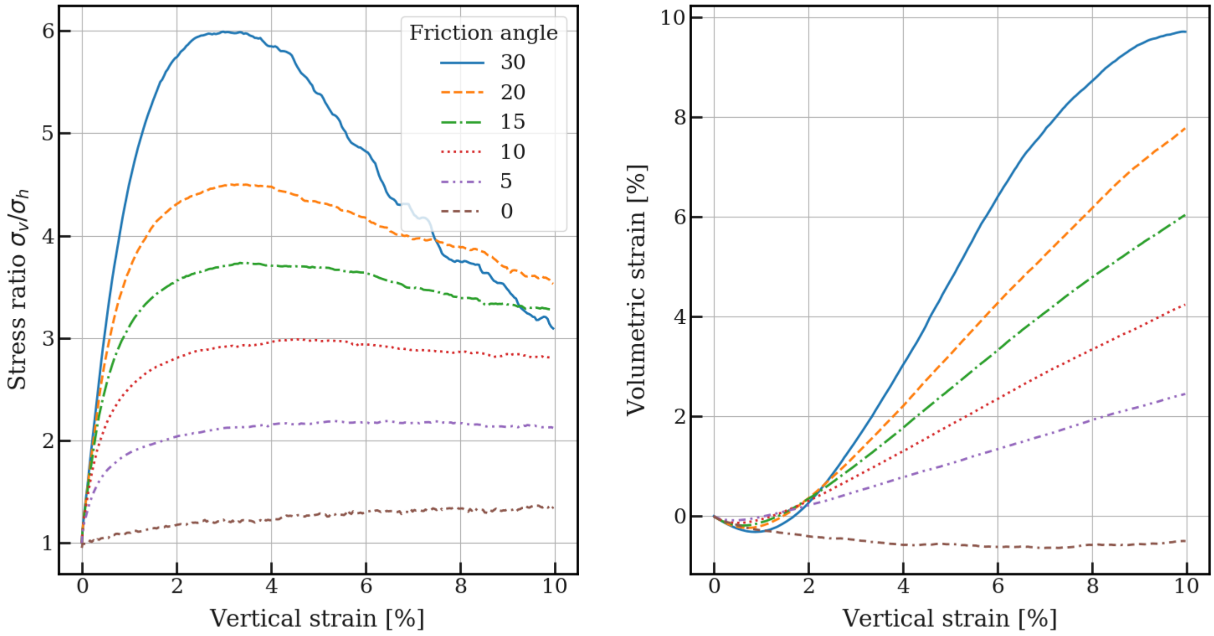

Figure 4.11: Calibration of interparticle friction using flexible boundaries.

Table 4.7: Peak friction angle with rigid boundaries.

Interparticle friction, μ	**Peak friction, φ_p**
30	46.7
20	40.4
15	36.2
10	30.5
5	22.3
0	8.2

Table 4.8: Peak friction angle with flexible boundaries.

Interparticle friction, μ	**Peak friction, φ_p**
30	45.6
20	39.5
15	35.5
10	29.9
5	21.9
0	8.8

Full roughness on loading platens

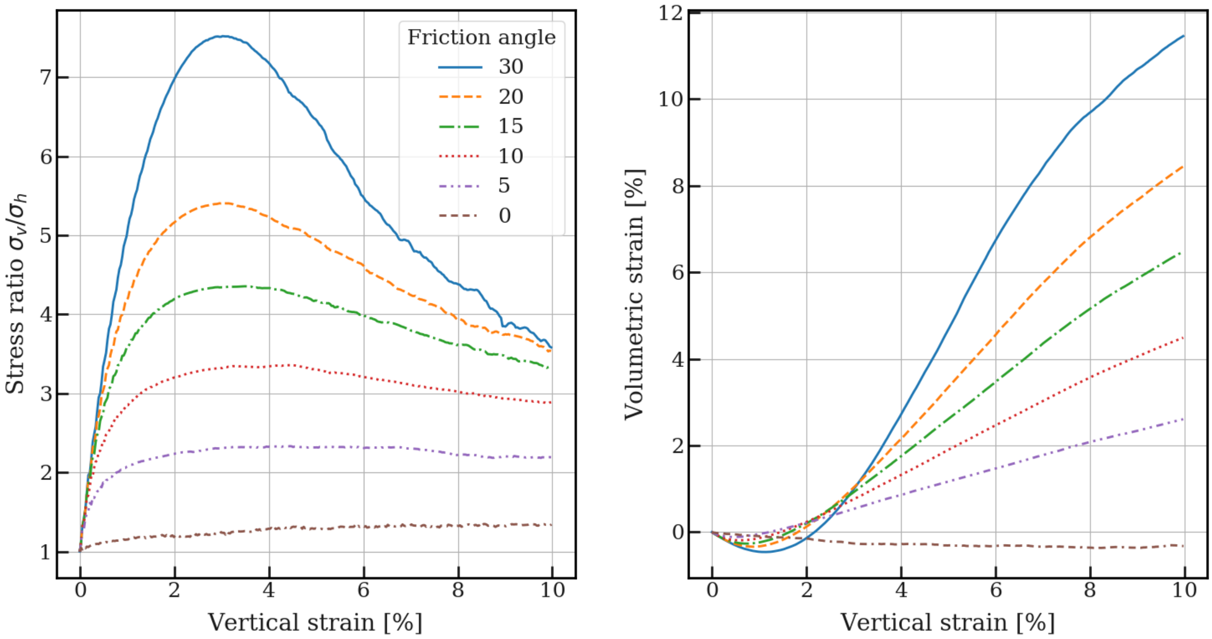

Figure 4.12: Calibration of interparticle friction using rigid wall boundaries. Full roughness on loading platens.

Table 4.9: Peak friction angle with rigid boundaries and rough loading platens.

Interparticle friction, μ	**Peak friction,** φ_p
30	49.8
20	43.3
15	38.6
10	32.5
5	23.3
0	8.2

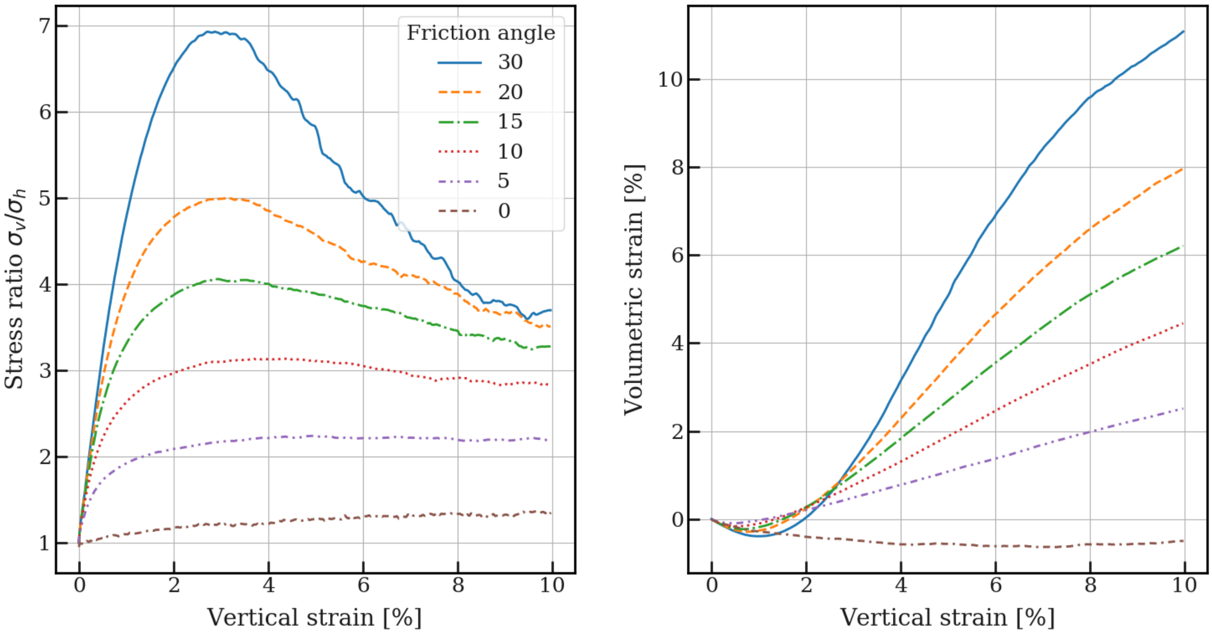

Figure 4.13: Calibration of interparticle friction using flexible boundaries. Full roughness on loading platens.

Table 4.10: Peak friction angle with flexible boundaries and rough loading platens.

Interparticle friction, μ	**Peak friction, φ_p**
30	48.4
20	41.8
15	37.2
10	31.1
5	22.5
0	8.8

Chapter 5

Shear Localisation Tests

The following chapter will present plane strain results performed with both rigid and flexible boundaries, with both rough and frictionless end conditions. A particular plane strain test with membrane boundaries and frictionless end conditions will be subjected to an in-depth analysis showcasing all the data extracted with the different data evaluation tools. The tests performed with rigid boundaries are primarily included to showcase the failure mechanisms resulting from the more restricted shear bands.

5.1 Method

For the shear localisation tests a 17,000 particle sample is generated. Particles are compacted isotropically by particle growth to 200kPa. The dimensions are 25 cm in height, 2cm in depth and 10cm in width.

Particle B has been used in all shear localisation tests due to the elongated particle geometry providing rotation resistance, in expectation of rotations and increased dilation in the shear band zone.

The stable, compacted sample show a uniform particle size increase from the generated cloud of 48.4% resulting in a mean grain radius of 1.63mm. The particle size distribution is uniform across 0.98mm to 2.3mm in equivalent radius.

At the selected interparticle friction, $\mu = 15°$, the maximum stable initial porosity obtained during compaction for the loose sample is 38.8% while the densest samples have a porosity of 32.2%.

The tests performed for visualizing shear banding are plane strain tests. The boundaries are flexible in the x-direction of the sample, with rigid plates in the z- and y-directions. Strain control of the plates in the y-direction is turned off for the plane strain tests. Confining stress is applied in the x directions, being perpendicular to initial undeformed membrane, but not perpendicularly to membrane surface as it deforms.

The cylinder connections in the membrane mesh are set at a normal stiffness of 400 N/m.

All tests are performed with frictionless interaction of the particles with the lateral confining walls and membranes. Both tests with full roughness and frictionless contact with the loading platens are performed.

All figures show the sample in the x-z plane. The figures with contact number development show a central 5mm slice of the sample in order to visualize the large dilatancy localised in the bands.

Volumetric expansion is given as positive in the strain plots.

The input parameters determined from the calibration tests and the literature review are included in table 5.1 below.

Table 5.1: Input parameters for shear localisation tests.

Input parameters	**Value**
Solid density [kg/m^3]	2800
Young [MPa]	200
Poisson	0.3
Compaction friction [°]	0-15
Internal friction [°]	15
Isotropic stress [kPa]	200
Damping [%]	3
Strain rate [%/sec]	40
Time step [sec]	6e-7

5.2 Results

5.2.1 Frictionless loading platens

Frictionless contacts of the loading platens at the sample ends. From figure 5.2 one can identify a number of interesting characteristics. For the dense sample, peak friction of 40.4°occurs at 2.4% strain at the maximum angle of dilation. Yield at 0.8% strain. The peak stress drops rapidly due to shear localisation. Peak dilatancy angle at the point of maximum plastic expansion is calculated to be, $\psi = 23.0°$.

The loose sample reaches peak friction of 28.9°at 7.0% strain. Yield at 3.2% strain. Loose sample stress development show no clear peak within the given strain range.

Dense sample

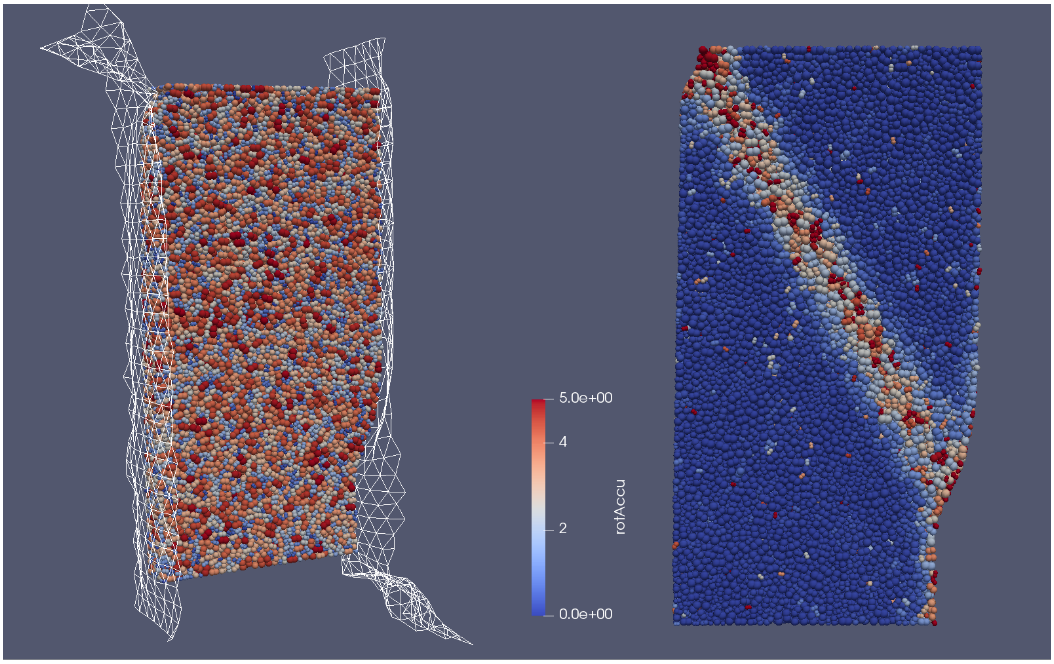

Figure 5.1: Sample at 10% strain. Showing fully deformed membrane mesh on the left and accumulated particle rotations on the right.

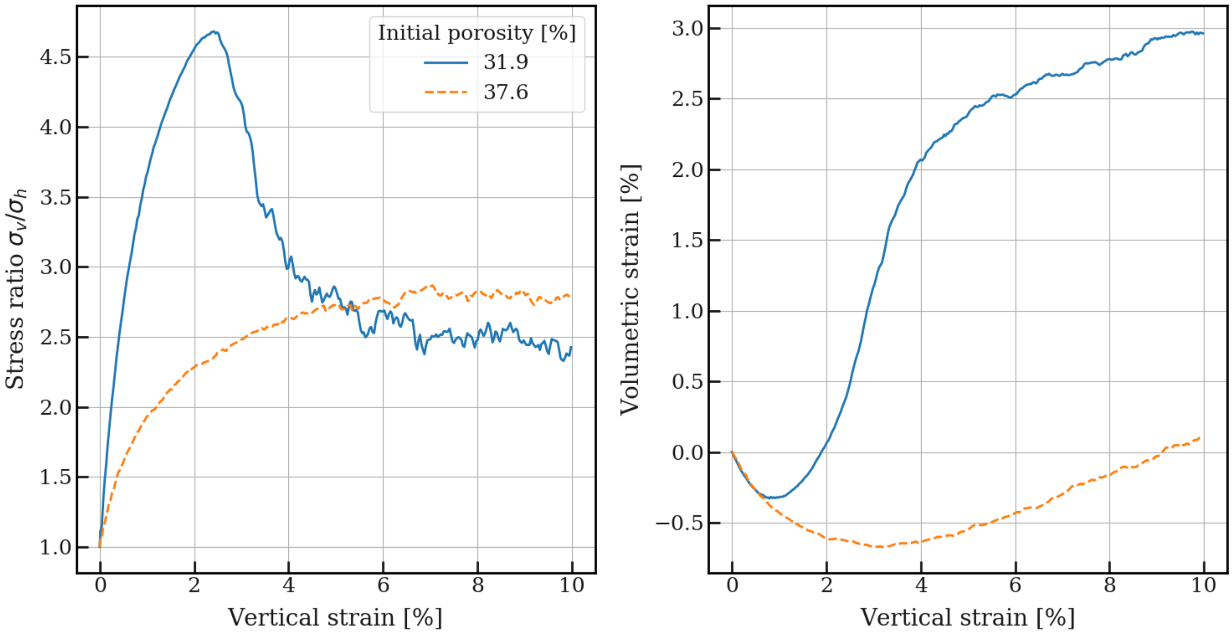

Figure 5.2: Dense and loose sample packing of particle B with flexible boundaries and frictionless platens.

Incremental particle rotations

Examining figure 5.3. At 2% strain the sample show finely spread shear bands throughout the sample before the peak at 2.4% strain. Immediately post peak, rotations are starting to concentrate in the failure mechanism shear band. And at 3% strain the rotations have concentrated fully to the shear band.
The orientation of the shear band with respect to the horisontal axis is approximately 58°.

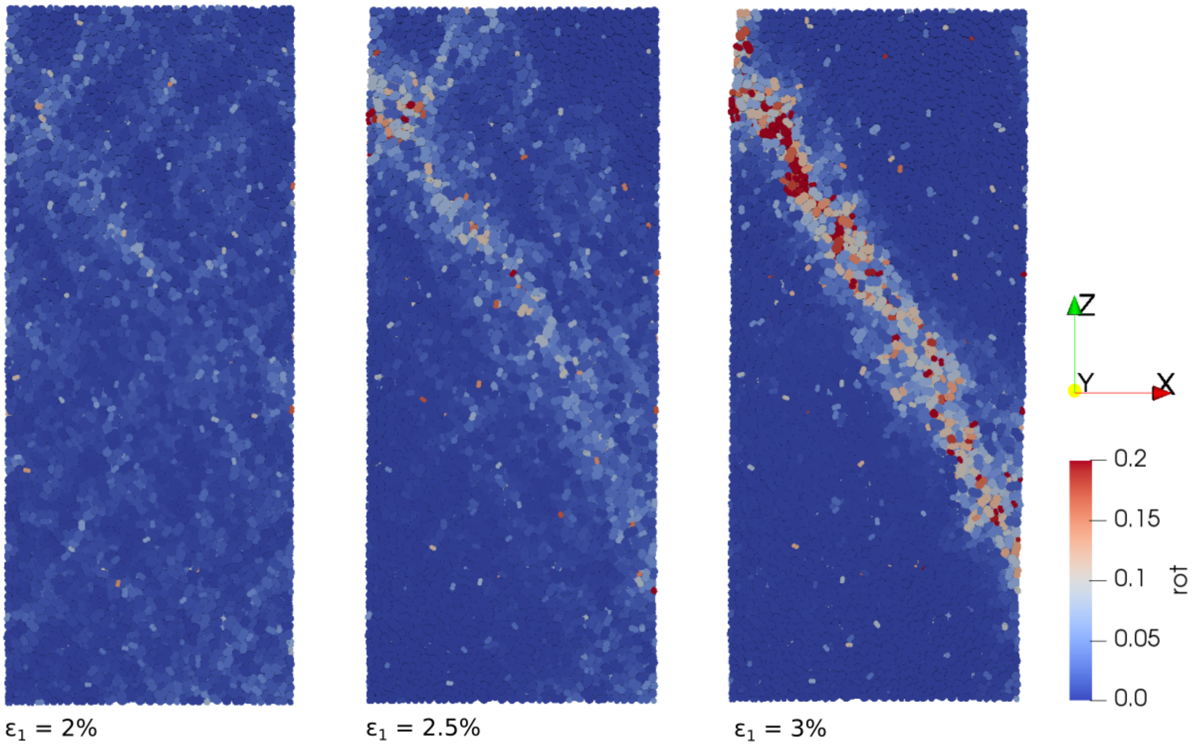

Figure 5.3: Incremental particle rotations at 2%, 2.5% and 3% vertical strain showing shear band development.

Incremental change of contact number

The pre peak behaviour show seemingly uniform distribution of dilation and contraction in the sample. When regarding the results in combination with the rotation tracking, the change in contacts seem to be localised in finely distributed shear bands throughout the sample.

At 2.5% strain, directly after peak at 2.4%, the sample show dilation starting to localise in the final shear band. From 2.5% to 3% strain further concentration occurs. At 7.5% strain large voids are clearly visible in especially the lower right portion of the band.

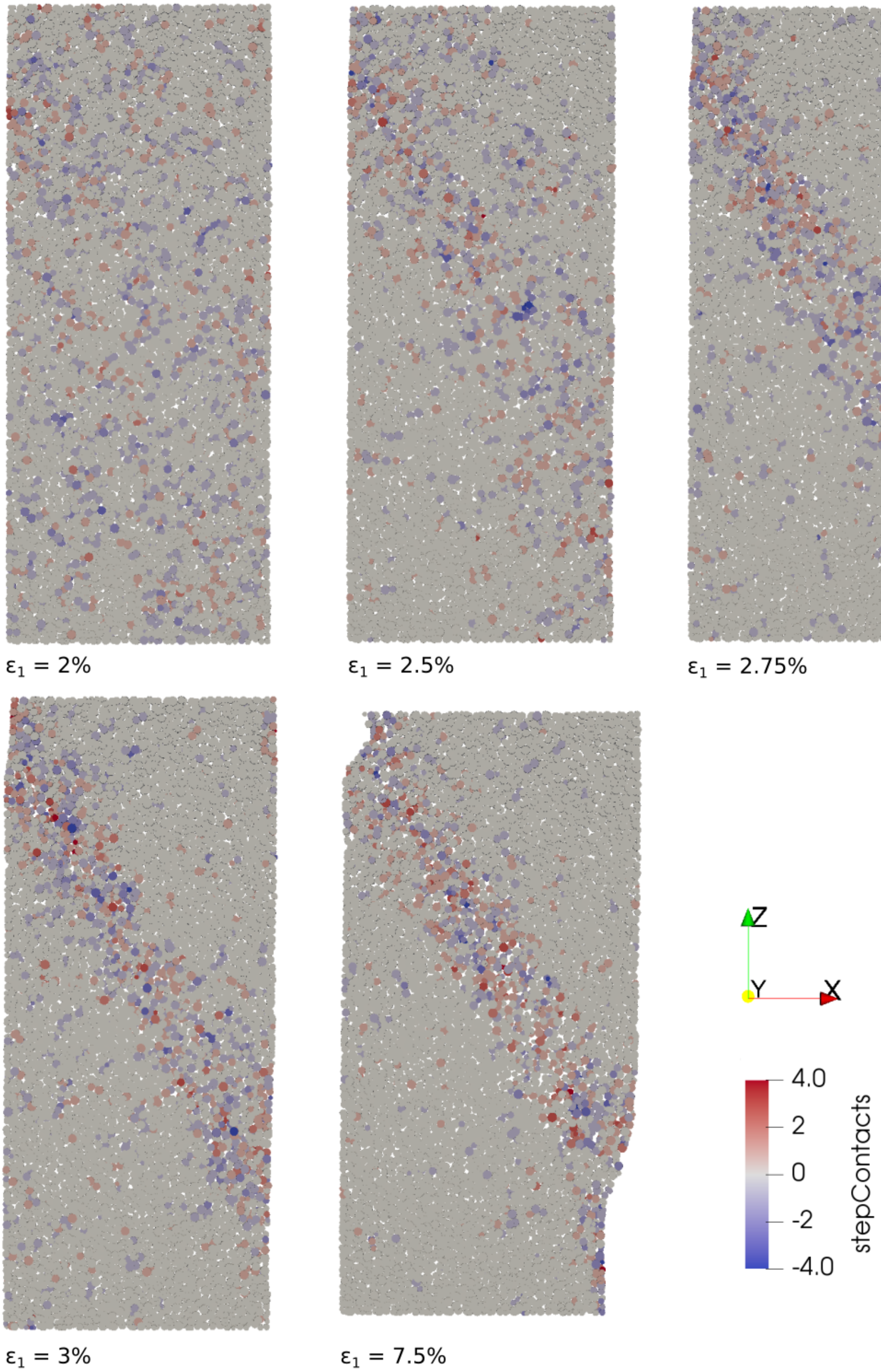

Figure 5.4: Incremental change in contact number for each 0.25% vertical strain.

Force chains
Examining figures 5.5 and 5.6. At 2% strain the force columns are uniformly distributed in the sample with the predominant orientation being in the principal stress direction. Directly post peak stress, at 3% one can observe the initial buckling of the columns, especially in the upper left of the sample. An increase in voids can be seen in this region, as well as rotated orientations of columns. Columns of high magnitude normal force are localised in the shear band resulting from the decreasing number of contacts.

As the columns buckle and the local porosity increases around the shear band, the number of strong contacts also decrease as can be seen at 4% strain in figure 5.6. The shear band region continues to have a lower density of force chains than pre preak, but at 7.5% strain the contacts increase again in the band.

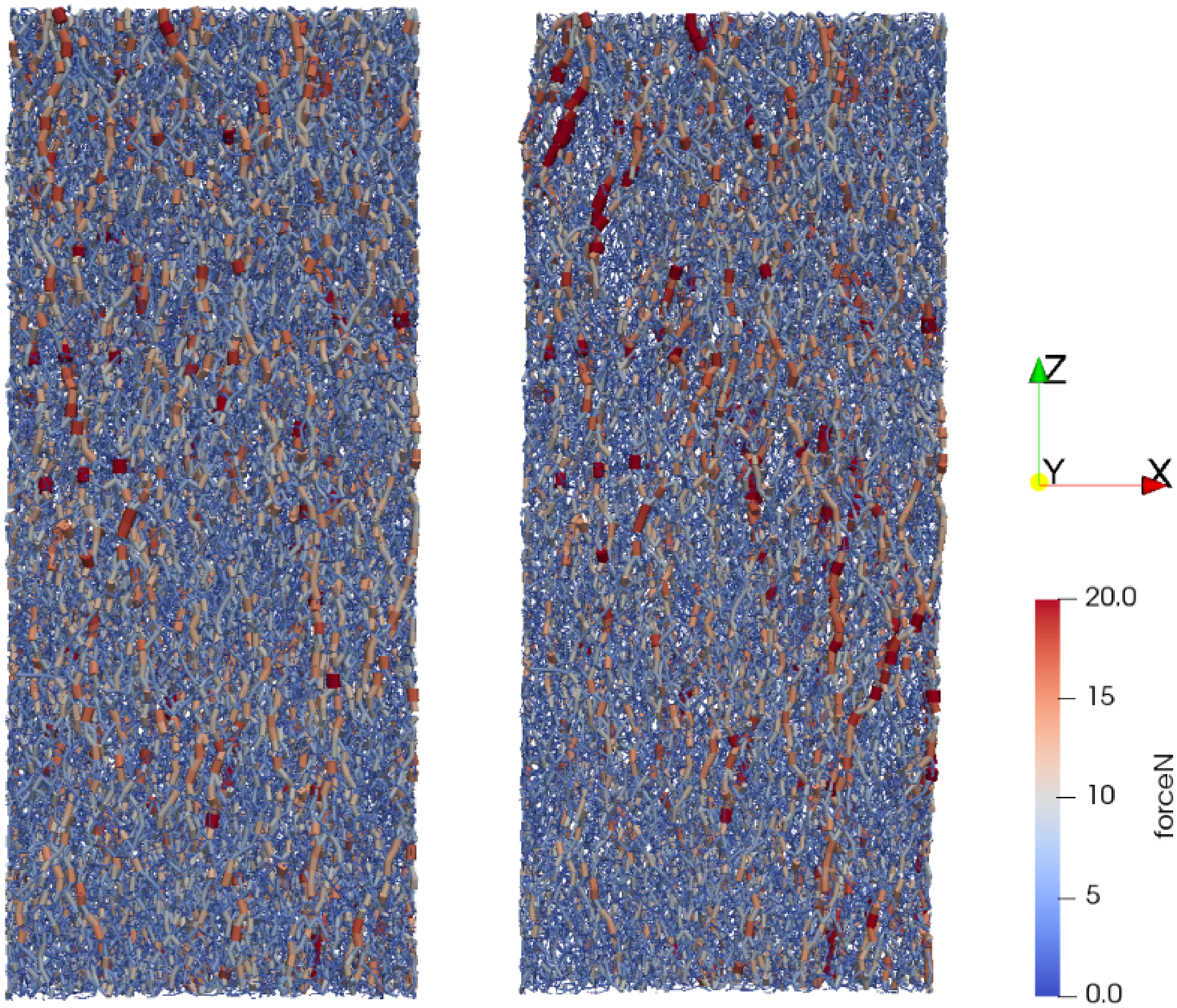

$\varepsilon_1 = 2\%$ $\varepsilon_1 = 3\%$

Figure 5.5: Force-chains at 2% and 3% vertical strain.

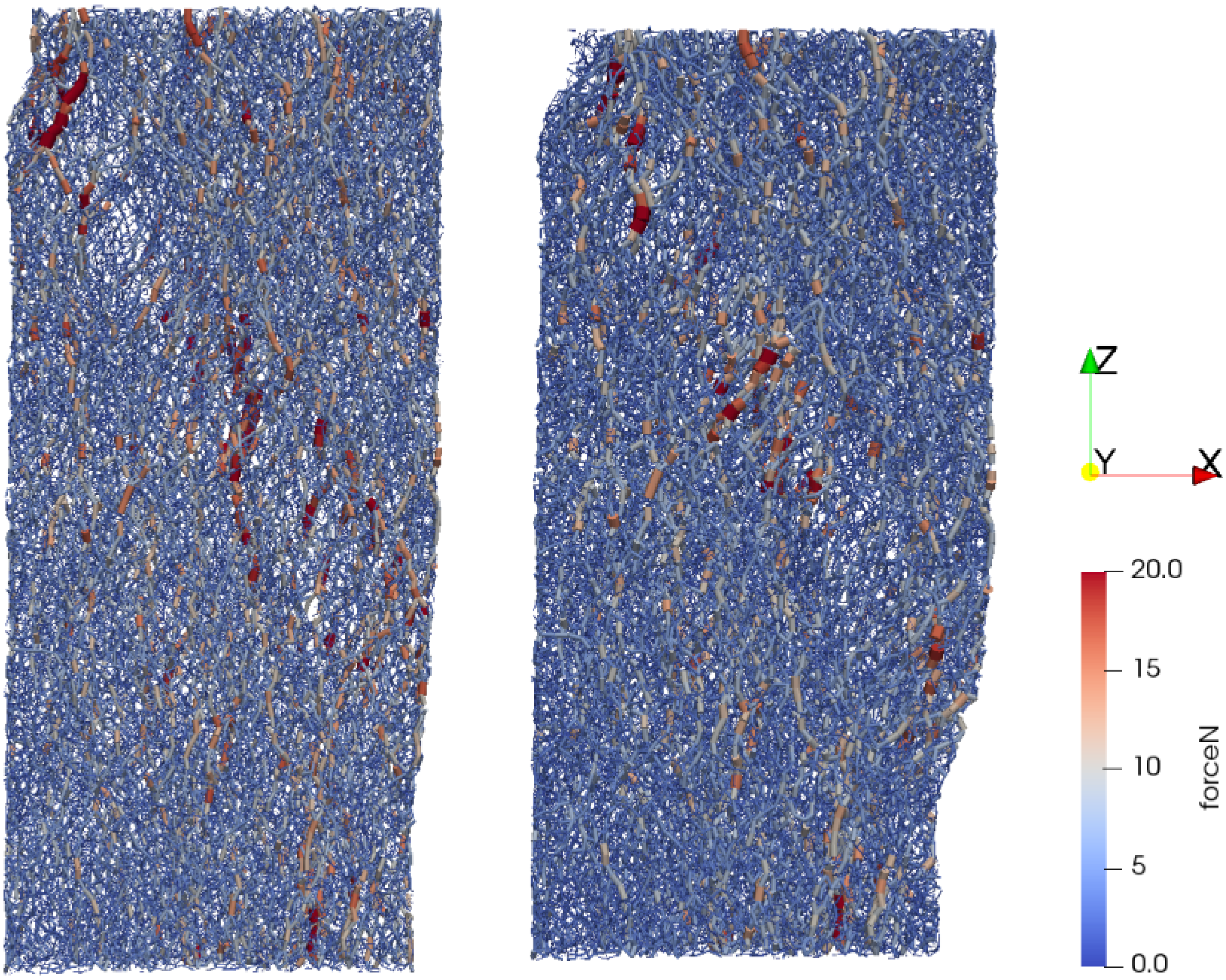

$\varepsilon_1 = 4\%$

$\varepsilon_1 = 7.5\%$

Figure 5.6: Force-chains at 4% and 7.5% vertical strain.

Particle pathlines

The measured shear band orientation from figure 5.7 is approximately 59°. $\varphi_p = 40.4°$ The Mohr Coloumb theory estimates this to be $\theta_C = 45° + \frac{\varphi_p}{2} = 65.2°$.

The Roscoe angle is given as $\theta_R = 45° + \frac{\psi}{2} = 56.5°$.

Arthur orientation, $\theta_A = 45° + \frac{\psi+\varphi_p}{4} = 60.9°$.

Measured shear band orientation is well aligned with the estimated Arthur orientation.

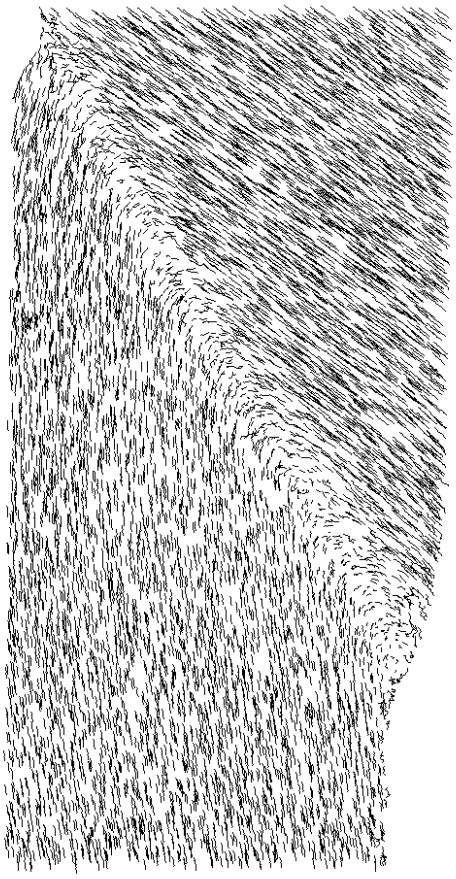

Figure 5.7: Particle pathlines at 10% strain.

5.2.2 Rough loading platens

Peak friction for dense sample corresponds to 40.7 °at 2.4% strain. Yield at 1.0% vertical strain. Peak friction for loose sample 30.7°at 9.3 % strain. Yielding occur at 2.6% strain. Peak is not clearly developed.

Maximum dilatancy angles of 21.5°and 6.0°for dense and loose samples respectively.

Primary shear band develops from top left to bottom right on figure 5.8. The secondary band is mostly developed after 7.5% strain.

Dense sample

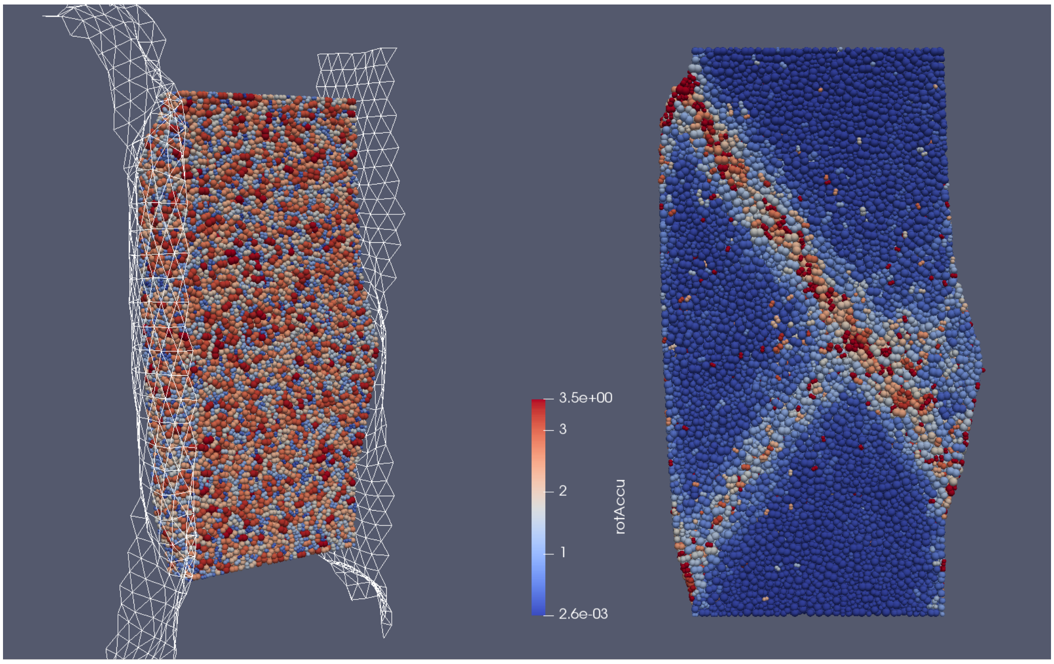

Figure 5.8: Sample at 10% strain. Showing fully deformed membrane mesh on the left and accumulated particle rotations on the right.

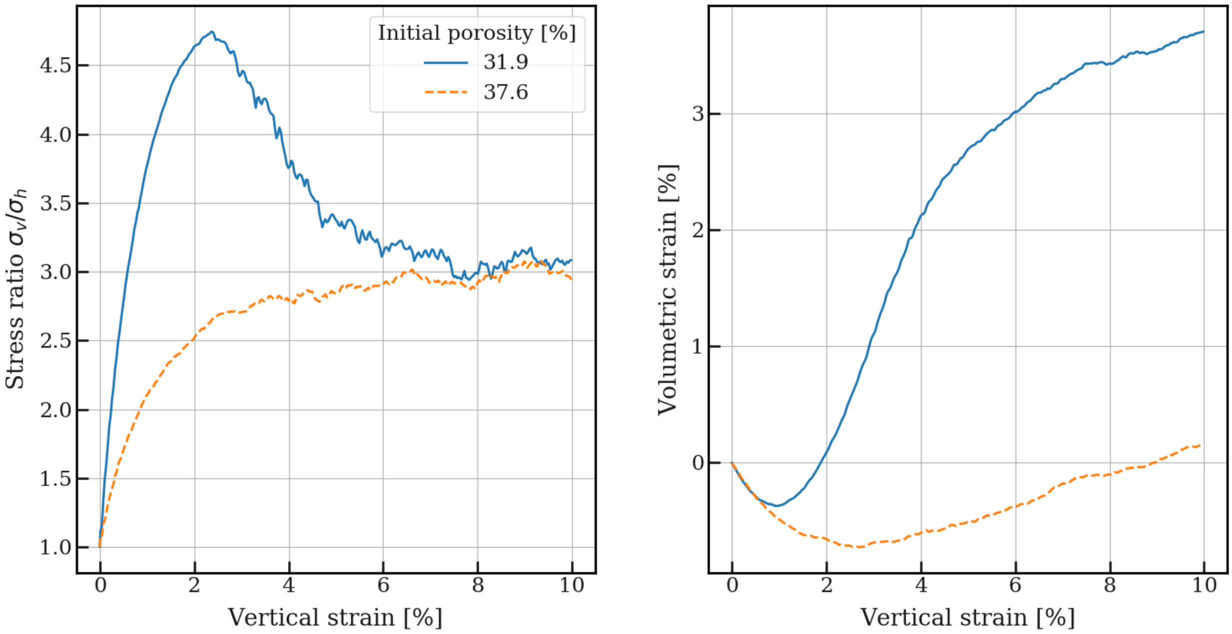

Figure 5.9: Dense and loose sample packing of particle B with flexible boundaries and rough platens.

Particle pathlines

The orientation of the lower left band is 52°with the horizontal axis. The primary band forms an inclination of 55°with the horizontal axis. When reaching the primary band the secondary band continues at a gentler inclination while the primary band continues in a straight line. The bands interact with each other creating an area of diffuse plastic deformation at the right hand side in figure 5.8.

The Mohr Coloumb theory estimates the orientation to be $\theta_C = 45° + \frac{\varphi_p}{2} = 65.4°$. The Roscoe angle is given as $\theta_R = 45° + \frac{\psi}{2} = 55.8°$. Arthur orientation, $\theta_A = 45° + \frac{\psi + \varphi_p}{4} = 60.6°$.

The orientation of the primary band is close to the estimated Roscoe orientation. The orientation of the secondary band is slightly outside the range of orientations proposed by theory.

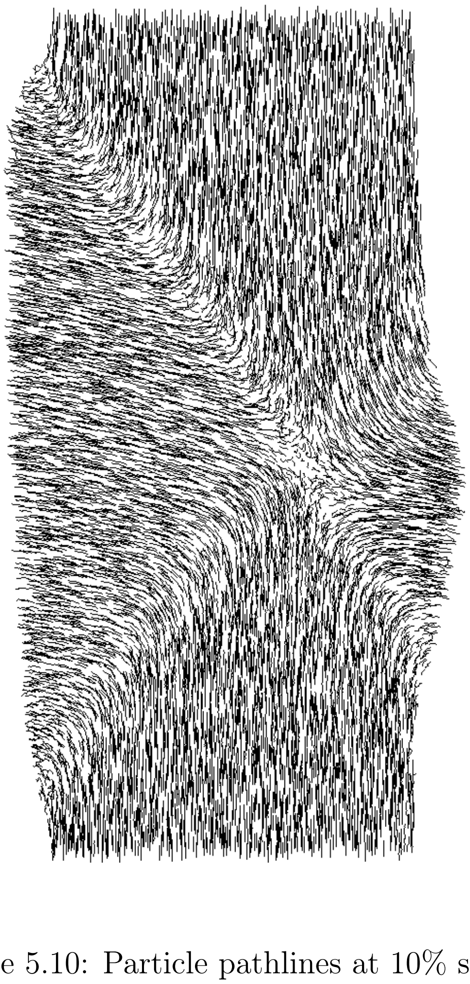

Figure 5.10: Particle pathlines at 10% strain.

5.2.3 Rigid boundaries

The tests with rigid boundaries show shear banding as well, but force bands to develop from the corners of the sample. The shear bands seem to be reflected from the boundaries in the cases with loose samples.

The rigid wall boundaries force the shear bands to cross diagonally from corner to corner of the dense sample. This restriction seem to increase compressive strength slightly for the rigid conditions compared to the flexible boundaries. Peak deviatoric stress of the rigid tests show a 6.7% increase over the tests with flexible with rough end conditions. With frictionless platens the peak deviatoric stress is increased by 9.0% compared to the flexible case.

The loose samples show finely dispersed lesser bands throughout the sample. Also show less accumulated rotation in these bands.

Frictionless loading platens

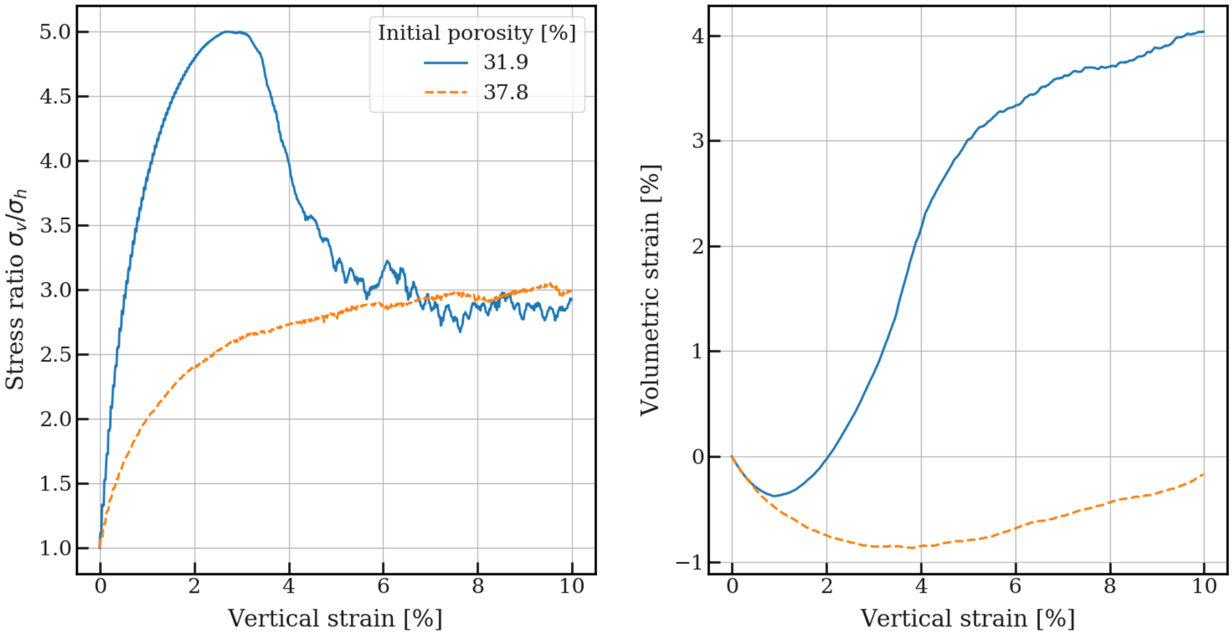

Figure 5.11: Sample response of dense and loose sample packing of particle B with rigid boundaries and frictionless platens.

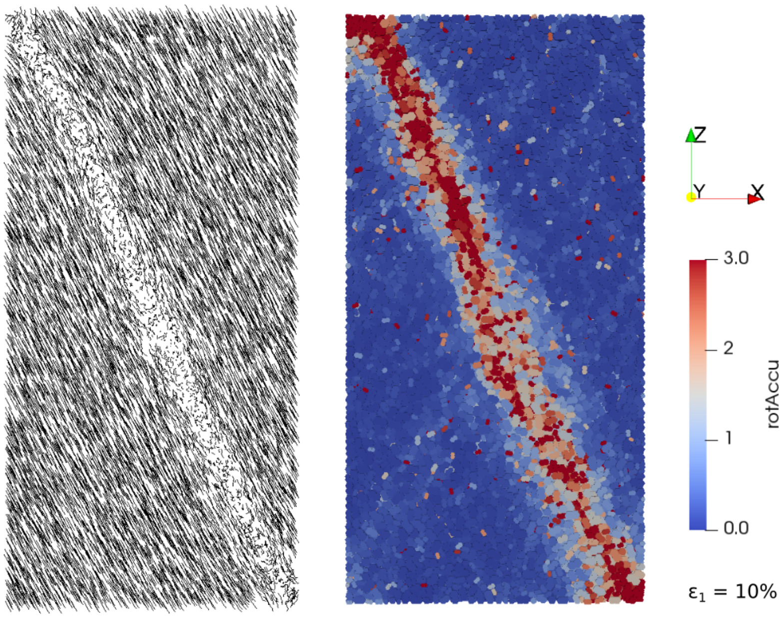

Figure 5.12: Particle pathlines and accumulated rotations for dense sample with rigid boundaries and no friction on loading platens.

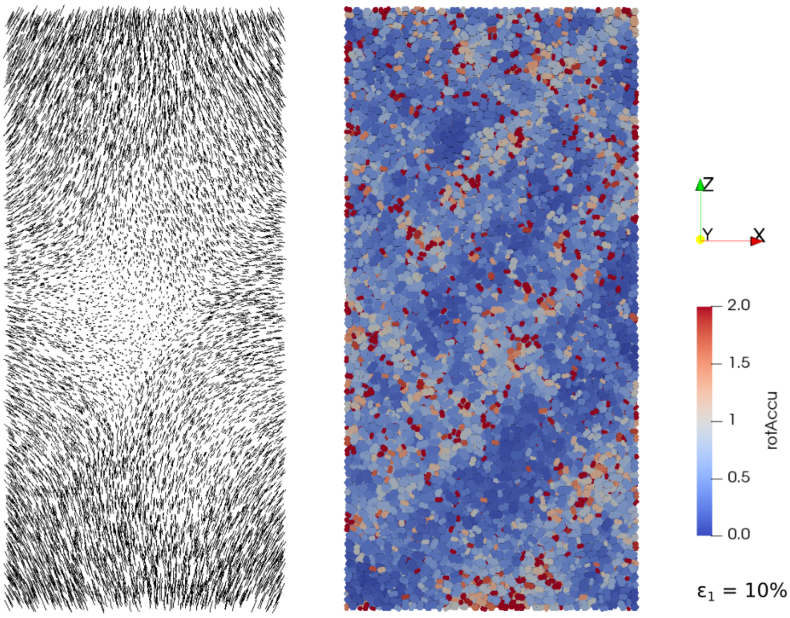

Figure 5.13: Particle pathlines and accumulated rotations for loose sample with rigid boundaries and no friction on loading platens.

Full roughness on loading platens

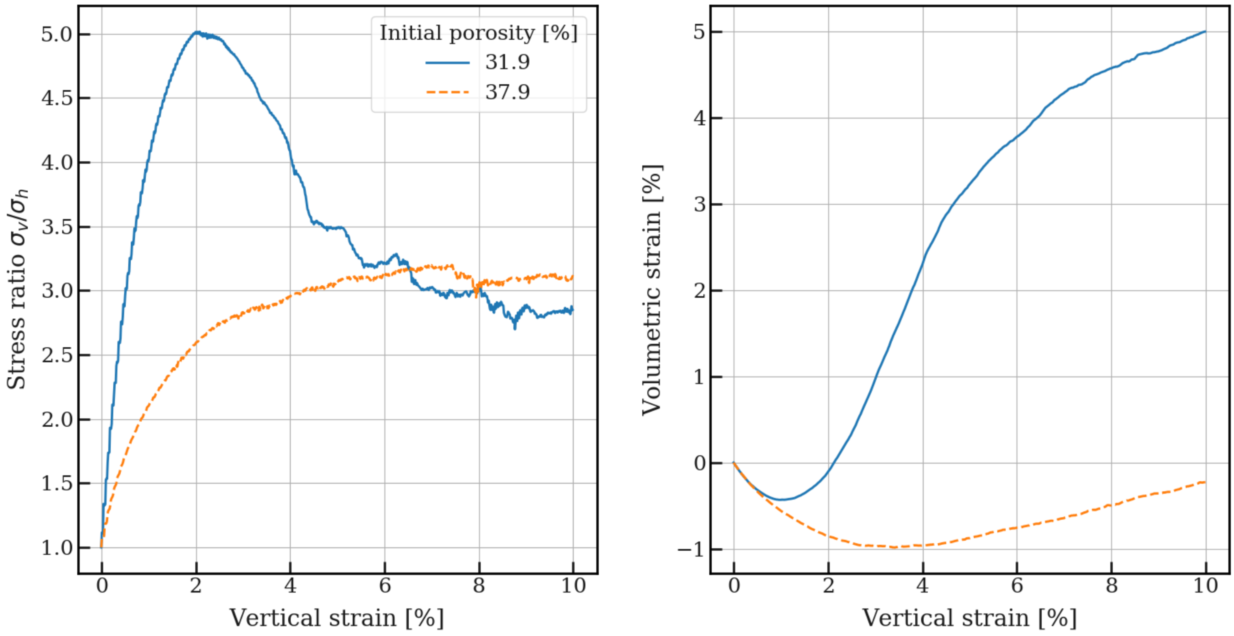

Figure 5.14: Sample response of dense and loose sample packing of particle B with rigid boundaries and rough platens.

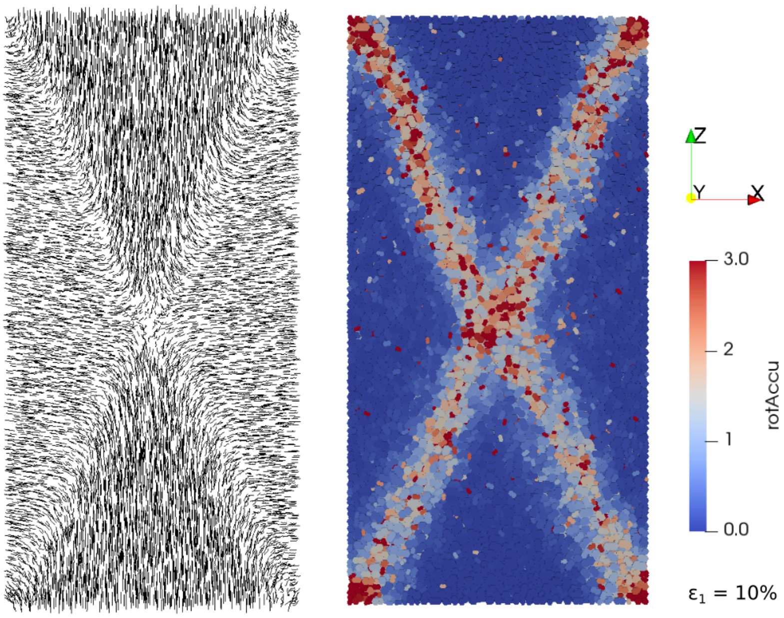

Figure 5.15: Particle pathlines and accumulated rotations for dense sample with rigid boundaries and full roughness on loading platens.

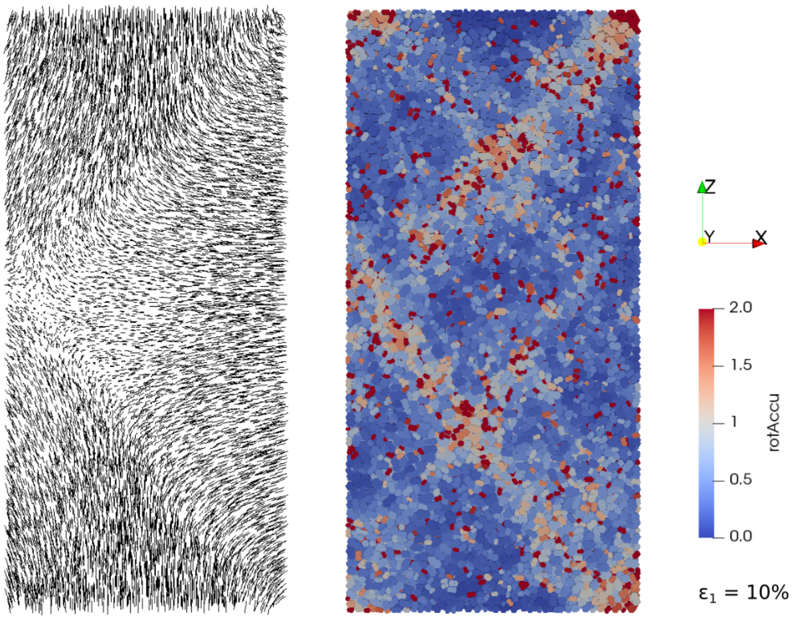

Figure 5.16: Particle pathlines and accumulated rotations for loose sample with rigid boundaries and full roughness on loading platens.

Chapter 6

General discussion

This section includes discussion of the results and methods that are generally applicable for all the performed tests.

Calibration results

The calibration procedure was performed for two reasons. It was made to determine parameters for the shear localisation tests, and also to reveal the influence of flexible boundaries on the measured macroscopic material response.

As lab performed triaxial tests both are performed with lubricated and rough end plates, the effect of friction on the sample ends were also examined. For the calibration results a frictionless interaction for the top and bottom load plates was expected to limit the tendency for shear banding associated with applied friction on the ends. This would lead to a more isotropic stress situation and uniform deformation of the sample, avoiding the "barreling"-phenomenon of conventional triaxial tests when using flexible boundaries. The tests show limited impact of the rough end conditions however. End friction showed increased peak friction angle associated with rotations of the principal stress leading to increased vertical capacity.

Due to time constraints during the project, calibration of the poisson ratio, was not performed. For the same reason the number of tests per parameter is limited. For establishing increased reliability of the parameter effects, a larger number of tests is required.

The difference in sample response on macroscopic stiffness and peak friction angle when comparing flexible and rigid boundaries is very limited. This suggests either shear banding in all of the tests or none, as localised failure is expected to impact the measured peak friction angle, which would lead to larger differences in stress-strain curves. These tests did however not include graphical data.

Shear localisation results

The test with frictionless platens and flexible boundaries show a singular shear band of thickness varying between 11 to 16 mean grain diameters. This is not in accordance with Bardet and Proubet (1991). Both of the planar tests show other behaviour according to the established theory about shear bands. The data show largely increased rotation and dilation in the shear zones. The buckling of force columns seem to be closely linked to the increased rotation seen in the bands, stemming from the "toppling over" and thereby rotations of the individual particles that are the constituents of each column.

Rotations are not measured correctly for three dimensional space, but is used as a measure of the rotations of particle relative to each other. It was chosen to not examine rotation about a specific axis, due to simulation of the sample in three dimensions. The rotations were expected to predominantly occur about the axis perpendicular to the sliding direction, but as the shear bands are three dimensional phenomena and not planes, rotation is also bound to occur about all axes.

The results presented are predominantly qualitative analysis relying heavily on visual interpretation of behaviour.

The tests are performed with a relatively low number of particles. This is primarily required due to the restrictions imposed by the membrane on the time step. The low particle number is thought to impact the data recovered from the shear band zones. With finer particle size distribution, the phenomena can be viewed at a higher resolution, potentially illuminating the behaviour further.

Up until the peak stress, minor shear bands are developed at gentler angles than the final shear mechanism. When reaching peak stress, the soil structure collapses onto one primary shear band, with potential secondary and tertiary bands as well. Further deformation is then strongly localised within these bands, with largely coherent soil blocks sliding on the bands.

By varying the end conditions the tests show different failure mechanisms in line with expected behaviour from theory. Frictionless and rough end conditions give the same peak strength. However, frictionless platens seem to induce more brittle behaviour in the samples due to very localised deformation in one singular band. The tests with rough platens accordingly show a less abrupt reduction of stress in the post-peak region suspected to be because of a somewhat higher stability in the failure mechanism of double bands.

The measured shear band orientation was well in line with the empirically derived Arthur orientation. With the relative low number of particles, and the diffuse shear band at the right in figure 5.4 there is some uncertainty in measured orientation.

Strain rate
The tests are performed at relatively high strain rates. However the shear band inclinations are at the lower ends of the estimated orientations. This suggests the strain rates are low enough to not lead to steepening of the shear band inclinations as dis-

cussed by Iskander et al. (2015).

The strain rate used in the tests can be considered quite high. It would be beneficial with a lower strain rate to ensure quasi-static conditions in the sample. The risk with a higher strain rate is that the grains are not allowed enough time to rearrange under the influence of the applied strain. This leads to increased measured stress, and impacts the plastic deformation. However, when considering the relative behaviour of the flexible and the rigid boundaries, it is assumed that both conditions are effected similarly such that comparison is still valid.

Boundary conditions
The triaxial tests with membranes only use membranes in two out of four lateral directions. This does of course have the potential of influencing the measured results. For the calibration of E modulus, the difference between the two boundary conditions is significant, especially with lubricated platens. As expected, the rigid boundaries limit the lateral deformation at the middle of the sample, leading to stiffer behaviour. With flexible bounds in all lateral directions, even softer behaviour is expected.

No tests using periodic boundaries were performed. These boundary conditions might be relevant for calibration purposes. Comparisons between sample response using periodic boundaries with flexible boundaries is also of interest. The periodic boundaries might behave more in line with flexible during uniform deformation as they are both stress controlled boundaries variable over the height. Shear banding is however suppressed in periodic conditions as they would form oblique to the periodic boundaries.

Membrane
Discrepancies in the results compared to expected physical behaviour may stem from some of the following simplifications:

- Force application on membrane perpendicular to y-z-plane, not perpendicularly to the membrane surface
- Membrane flexibility coupled with contact detection leading to too stiff membrane behaviour
- Membrane consisting of connected rigid elements

Keeping the direction of force application constant may have influenced sample response at large strain where the membrane deformation would lead to rotation of the force directions. The effect of this is considered to be low at lower strain levels, and also assumed to have only minor impact at larger strains.

Another issue with the static direction of applied force is slipping of the membrane at higher strains visible in figure 5.1. This is of course a consequence of the frictionless sample-membrane contact as well as the sloping surface of the sample at advanced stages of shear banding. At these strain levels, the results were not impacted due to the extended membrane surface above and below the sample. However, the loose samples were unable to reach strain levels higher than 10% before the membrane became unstable under these conditions.

As the membrane contact detection is coupled with the tensile stiffness of the membrane, the stiffness might impact shear band development at larger strains. The results in chapter 5 show a more diffuse band at the sample border with the highest membrane tension. The band is show a more diffuse contact number development as well as the distribution of large voids at the right hand side in figure 5.4. This seem to suggest a locally higher shear band thickness. Whether this is an artifact of high membrane stiffness is unknown.

The membrane is composed of individual rigid elements. It is therefore unable to deform precisely like a membrane with infinite degrees of freedom. However, the membrane mesh is considered fine enough to not effect the sample behaviour to any large extent.

Sample generation

The sample is not subjected to gravitational forces during preparation, possibly differentiating the sample fabric from empirical cases. The soil deposition is known to have a substantial effect on soil behaviour, more specifically on soil anisotropy. In the compaction phase, the confining stress is increased through particle growth and static wall boundaries. This leads to uniform sample fabric. Sample fabric is known to have an impact on strain localisation.

When comparing tests performed with rigid and flexible boundaries, the samples are generated and compacted identically. However, when inserting the compacted samples into the compressive tests, the sample is allowed to reach equilibrium within the confines of the membrane. Some plastic deformation is therefore assumed to occur prior to the deviatoric loading phase. Stability reasons and the change in geometry make it unfeasible to replicate the exact overlap between the membrane as with the rigid walls. This differs of course from the rigid walls, which are identical to the compaction phase boundaries.

Particle geometry

Particle A and B were used to simulate a particle of very limited and one with very high rotational resistance. The tests use simplified particle geometry in order to simulate a larger number of particles as roughness and rotational resistance of naturally occurring grains is very computationally expensive to emulate.

The geometry of particle B provide very large roughness. Thus it also shows very high dilatancy angle at relatively low interparticle friction as a consequence of this large roughness. Clump B seems to mimick rougher particles, but it is of a high degree of uncertainty what physical behaviour it is able to represent, and in what areas it is lacking compared to a real angular grains.

Chapter 7

Summary and conclusions

This chapter summarizes the findings in this thesis. They will be presented with respect to the objectives given in the introduction. Finally, suggestions for further work will be given.

Develop a flexible boundary condition for a cubic sample
The flexible boundary show promising results in regard to shear banding, with bands free to develop at the theoretically expected inclinations. The formation and development of the bands also comply with empirical observations of both laboratory performed compression tests and numerical simulations. Membrane performance is however hampered by the coupled contact detection and membrane stiffness. There were also stability issues at larger strains.

Determine the differences in rigid and flexible boundary conditions for compression tests
From the calibration results, it is implied that the addition of flexible borders have little effect on the measure peak friction angle. This is in line with the conclusions in the paper by Kozicki et al. (2013) that the calibration of macroscopic parameters are only slightly changed by the introduction of a flexible membrane. However, sample response is much stiffer with rigid boundaries. For the use of DEM in mimicking a particular real material, it is thus implied that the calibration procedure can be performed excluding flexible boundaries for determining peak friction angle. This simplifies the calibration process, as there today are limited flexible element solutions available in DEM-softwares. It should be noted however, the tests performed in this thesis are of a low particle number and with simple particle geometry, so further study is necessary.

Examine particle behaviour inside shear bands
The simulated model is capable of replicating the expected behaviour from the literature. The biaxial tests show behaviour congruent with theory in regards to dilation, rotation and force chains. Signs of force chain buckling lined up with shear band formation. The band orientation were in line with the empirically derived Arthur solution for the rough end conditions. The bands showed free development at low strains, but increased thickness at higher strains. Looser specimen show less localisation and more

finely dispersed lesser bands in the samples. This is also congruent with the lack of stress peak development.

Determine how load platen roughness influence the shear localisation development
The test results show significant influence of end conditions on shear band development. Rough and frictionless end conditions show almost identical peak stress, but different mechanisms of failure. Frictionless conditions show a more abrupt post peak stress reduction, suggesting brittle failure. With no friction at the platens, large lateral deformation occurs at the sample ends and the samples show both for rigid and flexible boundaries a tendency of developing singular clearly defined shear bands.

With rough platens, the sample ends are inhibited from sliding along the platens, leading to the development of two diagonally crossing shear bands. With rigid boundaries these mechanisms develop simultaneously, with no clear primary and secondary band. The flexible boundaries show development of one highly developed primary band and another secondary band. These show different orientations with the principal stress directions, with the primary band at a steeper angle.

7.1 Further work

The results shown in this thesis show the potential in the use of the Discrete Element Method. However, these simulations only utilise a limited part of DEM capabilities. As such, there is large room for further studies.

Shear localisation
Many of the properties dictating shear band behaviour is yet to be determined. Some topics of interest with regard to shear banding are:

- Effects of complex particle geometries
- Material models accounting for capillary forces
- Cohesive material models capable of describing the particle behaviour of finer material such as clays and silts.

Accuracy
In order to increase the accuracy of the generated results a couple of issues should be rectified: Firstly, the data capture intervals should be finer at strain points of interest. This entails running initial tests of a rough data capture resolution for identifying sample response warranting further scrutiny. Following this, more detailed data capture should be employed at the selected strain intervals.

Secondly, increase of particle number in the examined planes will increase the consistency of results as well as the resolution of observed particle behaviour.

Thirdly, the effect of the relatively high strain rates in this thesis should be examined further.

Membrane

For using a membrane of this design further refinement is recommended. In this regard, a number of considerations should be made:

Study the impact of fineness of the membrane mesh by varying the number of grid nodes.

Uncouple the stiffness of the membrane structure from the contact detection of the membrane. This may be achieved by examining the implementation of the area elements in Yade to alleviate the stability issues related to these elements or employ a software with this capability.

Another solution would be to use one of the other listed approaches for creating a flexible boundary. Of which, a robust equivalent force algorithm discussed in section 2.2.2 would be preferable.

Bibliography

Alshibli, K. A., & Sture, S. (2000). Shear band formation in plane strain experiments of sand. *Journal of Geotechnical and Geoenvironmental Engineering*, *126*(6), 495–503. https://doi.org/10.1061/(ASCE)1090-0241(2000)126:6(495)

Arthur, J. R. F., Dunstan, T., Al-Ani, Q. A. J. L., & Assadi, A. (1977). Plastic deformation and failure in granular media. *Géotechnique*, *27*(1), 53–74. https://doi.org/10.1680/geot.1977.27.1.53

Bardet, J.-P., & Proubet, J. (1991). A numerical investigation of the structure of persistent shear bands. *Geotechnique*, *41*, 599–613. https://doi.org/10.1680/geot.1991.41.4.599

Bourrier, F., Kneib, F., Chareyre, B., & Fourcaud, T. (2013). Discrete modeling of granular soils reinforcement by plant roots [Soil Bio- and Eco-Engineering: The Use of Vegetation to Improve Slope Stability]. *Ecological Engineering*, *61*, 646–657. https://doi.org/https://doi.org/10.1016/j.ecoleng.2013.05.002

Chareyre, B. (2007). Dem and geotechnical applications.

Chareyre, B., Cortis, A., Catalano, E., & Barthélemy, E. (2011). Pore-scale modeling of viscous flow and induced forces in dense sphere packings. *Transport in Porous Media*, *92*. https://doi.org/10.1007/s11242-011-9915-6

Cundall, P., & Strack, O. (1979). A discrete numerical model for granular assemblies. *Geotechnique*, *29*, 47–65. https://doi.org/10.1680/geot.1979.29.1.47

Desrues, J., & Andò, E. (2015). Strain localisation in granular media [Granular physics / Physique des milieux granulaires]. *Comptes Rendus Physique*, *16*(1), 26–36. https://doi.org/https://doi.org/10.1016/j.crhy.2015.01.001

Effeindzourou, A., Chareyre, B., Thoeni, K., Giacomini, A., & Kneib, F. (2016). Modelling of deformable structures in the general framework of the discrete element method. *Geotextiles and Geomembranes*, *44*(2), 143–156. https://doi.org/https://doi.org/10.1016/j.geotexmem.2015.07.015

Eliáš, J. (2014). Simulation of railway ballast using crushable polyhedral particles. *Powder Technology*, *264*, 458–465. https://doi.org/https://doi.org/10.1016/j.powtec.2014.05.052

Iskander, M., Omidvar, M., & Bless, S. (2015). Chapter 2 - behavior of granular media under high strain-rate loading (M. Iskander, S. Bless, & M. Omidvar, Eds.). In M. Iskander, S. Bless, & M. Omidvar (Eds.), *Rapid penetration into granular media*. Oxford, Elsevier. https://doi.org/https://doi.org/10.1016/B978-0-12-800868-3.00002-X

Iwashita, K., & Oda, M. (1998). Rolling resistance at contacts in simulation of shear band development by dem. *Journal of Engineering Mechanics*, *124*(3), 285–292. https://doi.org/10.1061/(ASCE)0733-9399(1998)124:3(285)

Kawamoto, R., Andò, E., Viggiani, G., & Andrade, J. (2017). All you need is shape: Predicting shear banding in sand with ls-dem. *Journal of the Mechanics and Physics of Solids*, *111*. https://doi.org/10.1016/j.jmps.2017.10.003

Kozicki, J., Niedostatkiewicz, M., Tejchman, J., & Muhlhaus, H.-B. (2013). Discrete modelling results of a direct shear test for granular materials versus fe results. *Granular Matter*, *15*(5), 607–627. https://doi.org/10.1007/s10035-013-0423-y

Kozicki, J., Tejchman, J., & Mróz, Z. (2012). Effect of grain roughness on strength, volume changes, elastic and dissipated energies during quasi-static triaxial compression using dem. *Granular Matter*, *14*. https://doi.org/10.1007/s10035-012-0352-1

Kozicki, J., Tejchman, J., & Mühlhaus, H.-B. (2014). Discrete simulations of a triaxial compression test for sand by dem. *International Journal for Numerical and Analytical Methods in Geomechanics*, *38*(18), 1923–1952. https://doi.org/10.1002/nag.2285

Kruyt, N., & Rothenburg, L. (2006). Shear strength, dilatancy, energy and dissipation in quasi-static deformation of granular materials. *Journal of Statistical Mechanics: Theory and Experiment*, *2006*, P07021. https://doi.org/10.1088/1742-5468/2006/07/P07021

Kuhn, M. R. (2017). 4 - loading, movement, and strength (M. R. Kuhn, Ed.). In M. R. Kuhn (Ed.), *Granular geomechanics*. Elsevier. https://doi.org/https://doi.org/10.1016/B978-1-78548-071-3.50004-9

Løvdahl, E. (2020). An introduction to the discrete element method implementation in the open-source software yade.

Marachi, N., Duncan, J., Chan, C., & Seed, H. (1981). Plane-strain testing of sand, In *Laboratory shear strength of soil*. ASTM International. https://doi.org/https://doi.org/978-0-8031-4806-2

Oda, M., & Kazama, H. (1998). Microstructure of shear bands and its relation to the mechanisms of dilatancy and failure of dense granular soils. *Géotechnique*, *48*(4), https://doi.org/10.1680/geot.1998.48.4.465, 465–481. https://doi.org/10.1680/geot.1998.48.4.465

Oda, M., Konishi, J., & Nemat-Nasser, S. (1982). Experimental micromechanical evaluation of strength of granular materials: Effects of particle rolling. *Mechanics of Materials*, *1*(4), 269–283. https://doi.org/https://doi.org/10.1016/0167-6636(82)90027-8

Peters, J., Lade, P., & Bro, A. (1988). Shear band formation in triaxial, and plane strain tests, advanced triaxial testing of soil, and rock, astm 977. *American Society for Testing Materials*, 604–627.

Qu, T., Feng, Y., Wang, Y., & Wang, M. (2019). Discrete element modelling of flexible membrane boundaries for triaxial tests. *Computers and Geotechnics*, *115*, 103154. https://doi.org/https://doi.org/10.1016/j.compgeo.2019.103154

Roscoe, K. H. (1970). The influence of strains in soil mechanics. *Géotechnique*, *20*(2), https://doi.org/10.1680/geot.1970.20.2.129, 129–170. https://doi.org/10.1680/geot.1970.20.2.129

Salot, C., Gotteland, P., & Villard, P. (2009). Influence of relative density on granular materials behavior: Dem simulations of triaxial tests. *Granular Matter*, *11*, 221–236. https://doi.org/10.1007/s10035-009-0138-2

Schanz, T., & Vermeer, P. (1996). Angles of friction and dilatancy of sand. *Géotechnique*, *46*, No. 1, 145–151. https://doi.org/10.1680/geot.1996.46.1.145

Šmilauer, V., & Chareyre, B. (2015). Dem formulation. https://doi.org/10.5281/zenodo.34044

Suzuki, K., & Yamada, T. (2006). Double strain softening and diagonally crossing shear bands of sand in drained triaxial tests. *International Journal of Geomechanics*, *6*(6), 440–446. https://doi.org/10.1061/(ASCE)1532-3641(2006)6:6(440)

Thornton, C. (2000). Numerical simulations of deviatoric shear deformation of granular media. *Géotechnique*, *50*(1), 43–53. https://doi.org/10.1680/geot.2000.50.1.43

Tong, A.-T., Catalano, E., & Chareyre, B. (2012). Pore-scale flow simulations: Model predictions compared with experiments on bi-dispersed granular assemblies. *Oil Gas Sci. Technol. - Rev. IFP Energies nouvelles*, *67*(5), 743–752. https://doi.org/10.2516/ogst/2012032

Tu, X., & Andrade, J. (2008). Criteria for static equilibrium in particulate mechanics computations. *International Journal for Numerical Methods in Engineering*, *75*, 1581–1606. https://doi.org/10.1002/nme.2322

Vardoulakis, I., Goldscheider, M., & Gudehus, G. (1978). Formation of shear bands in sand bodies as a bifurcation problem. *International Journal for Numerical and Analytical Methods in Geomechanics*, *2*(2), 99–128. https://doi.org/10.1002/nag.1610020203